Hydrological and geological controls for the joint evolution of dissolved oxygen and iron in crystalline rocks

Ivan Osorio-Leon[1], Camille Bouchez[2], Eliot Chatton[3], Nicolas Lavenant[4], Laurent Longuevergne[5], and Tanguy Le Borgne[3]

[1]University of Rennes 1
[2]Rennes Université
[3]Université de Rennes 1
[4]Geosciences Rennes
[5]CNRS - Université Rennes 1

November 24, 2022

Abstract

Dissolved Oxygen (DO) plays a key role in reactive processes and microbial dynamics in the critical zone. While the general view is that oxygen is rapidly depleted in soils and that deeper compartments are anoxic, recent observations showed that fractures can provide rapid pathways for deep oxygen penetration, triggering unexpected biogeochemical processes. As it is transported in the subsurface, DO reacts with electron donors, such as Fe^{2+} coming from mineral dissolution, hence influencing rock-weathering. Yet, little is known about the factors controlling the spatial heterogeneity and distribution of oxygen with depth. Here we present analytical expressions describing the coupled evolution of DO and Fe^{2+} as a function of fluid travel time in crystalline rocks. Our model, validated with reactive transport simulations, predicts a linear decay of DO with time, followed by a rapid non-linear increase of Fe^{2+} concentrations up to an equilibrium state. Relative effects of the reducing capacity of the bedrock and of transport velocity are quantified through a Damkohler number, capturing key hydrological and geological controls of Fe^{2+} and DO distributions in the subsurface. This framework is used to investigate contrasted DO and Fe^{2+} concentrations observed in two crystalline catchments. These differences are explained by the Damkohler number: one system is reaction-limited while the second is transport-limited. We show that hydrological and geological drivers can be discriminated by analyzing both O$_2$ and Fe^{2+}. These findings provide a new conceptual framework to understand and predict the evolution of DO in the subsurface, a key element in the critical zone.

Hydrological and geological controls for the joint evolution of dissolved oxygen and iron in crystalline rocks

Ivan Osorio-Leon[1], Camille Bouchez[1], Eliot Chatton[1], Nicolas Lavenant[1], Laurent Longuevergne[1], Tanguy Le Borgne[1]

[1]Univ Rennes – CNRS, Géosciences Rennes - UMR 6118. Rennes, France

Key Points:

- We derive and validate analytical expressions to predict the joint evolution of dissolved O_2 and Fe^{2+} in crystalline rocks.
- We show that the hydrological and geological controls can be discriminated by analyzing both O_2 and Fe^{2+} as a function of depth.
- The modeling framework is used to analyze O_2 and Fe^{2+} data on two sites with contrasted chemical properties.

Corresponding author: Ivan Osorio-Leon, `ivan-david.osorio-leon@univ-rennes1.fr`

Corresponding author: Camille Bouchez, `camille.bouchez@univ-rennes1.fr`

Abstract

Dissolved Oxygen (DO) plays a key role in reactive processes and microbial dynamics in the critical zone. While the general view is that oxygen is rapidly depleted in soils and that deeper compartments are anoxic, recent observations showed that fractures can provide rapid pathways for deep oxygen penetration, triggering unexpected biogeochemical processes. As it is transported in the subsurface, DO reacts with electron donors, such as Fe^{2+} coming from mineral dissolution, hence influencing rock-weathering. Yet, little is known about the factors controlling the spatial heterogeneity and distribution of oxygen with depth. Here we present analytical expressions describing the coupled evolution of DO and Fe^{2+} as a function of fluid travel time in crystalline rocks. Our model, validated with reactive transport simulations, predicts a linear decay of DO with time, followed by a rapid non-linear increase of Fe^{2+} concentrations up to an equilibrium state. Relative effects of the reducing capacity of the bedrock and of transport velocity are quantified through a Damköhler number, capturing key hydrological and geological controls of Fe^{2+} and DO distributions in the subsurface. This framework is used to investigate contrasted DO and Fe^{2+} concentrations observed in two crystalline catchments. These differences are explained by the Damköhler number: one system is reaction-limited while the second is transport-limited. We show that hydrological and geological drivers can be discriminated by analyzing both O_2 and Fe^{2+}. These findings provide a new conceptual framework to understand and predict the evolution of DO in the subsurface, a key element in the critical zone.

Plain Language Summary

In the critical zone, dissolved Oxygen (DO) is involved in pivotal biogeochemical reactions, such as the aerobic respiration of microbes, rock-weathering or contaminant degradation. The general view is that the deeper subsurface of continents is mostly anoxic. However, recent observations have shown that preferential flowpaths in rock fractures can favor oxygen penetration, thus extending deeper the influence of oxygen in reactions. Here, we present a modeling framework validated with field data to understand and predict the hydrological and geological controls on dissolved oxygen evolution in crystalline rocks, shedding new light on its influence on rock-weathering and microbial life in the critical zone.

1 Introduction

Oxygen is central in redox reactions because it the most abundant and readily available electron acceptor in the environment (Korom, 1992; Stumm & Morgan, 1996) and offers a strong redox potential. In aquatic environments, dissolved oxygen (DO) is mostly produced by photosynthesis and consumed by aerobic respiration of organic matter (Mader et al., 2017). In the subsurface, the transport of DO and CO_2 by fluid flow triggers the weathering of crystalline rocks (Fletcher et al., 2006; Kim et al., 2017; Li et al., 2017; Singha & Navarre-Sitchler, 2022), which represent a quarter of the outcropping Earth rocks (Hartmann & Moosdorf, 2012). The cycle of DO is thus closely related to the geochemical cycles of carbon (Petsch et al., 2004; Bar-on et al., 2018), iron (Melton et al., 2014; Napieralski et al., 2019; Kappler et al., 2021) and sulfur (Gu et al., 2020). Moreover, recent studies have pointed out that redox reactions, particularly involving DO, are often mediated by microbes (Erable et al., 2012; Napieralski et al., 2019; Kappler et al., 2021) because the redox potential of the reaction offers an energy source for microbes to thrive (Emerson et al., 2010). DO thus also exerts a key ecological role by impacting the biodiversity (Malard & Hervant, 1999; Hancock et al., 2005; Humphreys, 2009) and activity of aerobic microbial metabolisms (Druschel et al., 2008; Mader et al., 2017; Maisch et al., 2019).

When DO is not depleted in soils, either because of a limited soil-thickness or a low organic matter availability, oxic water can enter the bedrock and react with the electron donors available in the subsurface, such as $Fe(II)$, $Mn(II)$, CH_4, H_2 or HS^- (Kartsen Pedersen, 1997; Tebo et al., 2005). Iron is the most abundant redox-sensitive element in the Earth crust (Frey & Reed, 2012), it is linked to biogeochemical cycles of carbon, sulphur and nitrogen (Casar et al., 2021). The reduction of DO by iron can occur either by Fe(II)-sites on mineral surfaces (White et al., 1985) or by Fe^{2+} dissolved in water subsequently to the release of structural Fe(II) by mineral dissolution (White & Yee, 1985). The most common Fe(II)-bearing primary minerals in hard-rocks are silicates such as biotite (Malmström et al., 1996; Aquilina et al., 2018; Holbrook et al., 2019; Hampl et al., 2021), pyroxene (Behrens et al., 2015) and hornblende (Fletcher et al., 2006) and in less proportion, sulfates such as Pyrite (Gu et al., 2020).

Several field works documenting weathering profiles in hard-rocks, either from outcrops (Antoniellini et al., 2017) or borehole cores (Dideriksen et al., 2010; Bazilevskaya et al., 2013; Holbrook et al., 2019; Hampl et al., 2021), have suggested that DO transport by subsurface flow could explain the presence of secondary minerals and weathering induced fracturing (WIF) in ferrous silicates (Bazilevskaya et al., 2013; Kim et al., 2017) from deep regolith. Likewise, evidence from field measurements in fractured-rock aquifers has shown that DO can effectively persist in deep aquifers(Winograd & Robertson, 1982; Edmunds et al., 1984; Bucher et al., 2009; DeSimone et al., 2014; Sullivan et al., 2016; Ruff et al., 2022). Based on field observations, the presence or absence of DO in the subsurface has been attributed to lithological differences of the bedrock (Winograd & Robertson, 1982; Malard & Hervant, 1999). However, it is still challenging to predict the expected depth of dissolved oxygen in crystalline rocks as a function of lithology.

Fractures can provide fast transport pathways in the subsurface and therefore influence reactive transport processes (Deng & Spycher, 2019). The transport and fate of DO in fractured rocks have been studied in the framework of risk assessments for DO penetration to nuclear waste repository sites. Numerical studies have simulated the advance of the redox front in the matrix of granitic rocks (Macquarrie et al., 2010; Trinchero, Molinero, et al., 2018; Trinchero et al., 2019) and in fracture networks (Trinchero, Sidborn, & Puigdomenech, 2018) providing insights into the mechanisms driving oxygen transport in fractured rocks. Approximate analytical solutions have been obtained (Sidborn & Neretnieks, 2007, 2008) by assuming that the dissolution of Fe(II) bearing minerals is rapid compared to transport, which is relevant for large time scales (thousands of years). For smaller time scales, oxygen transport and reaction is controlled by the interplay between the characteristic dissolution rates and transport time scales (Trinchero, Sidborn, & Puigdomenech, 2018). However, this effect is not quantified analytically for the joint evolution of DO and Fe^{2+} concentrations, which limits current understanding of the hydrological and geological controls on oxygen depth distribution in the subsurface.

The interplay between transport and reaction rates at catchment scale has been conceptualized using the Damköhler number, defined as the ratio of the characteristic transport and reaction time scales (Maher, 2010; Maher & Chamberlain, 2014). In this approach, structures such as fractures and rock matrix are not represented explicitly but instead integrated into an effective fluid travel time, representing the time during which fluid has been exposed to reactive minerals (Seeboonruang & Ginn, 2006).

In this study, we use a travel time formulation to develop approximate analytical solutions for coupled DO and Fe^{2+} transport and reaction in the subsurface. We formulate the geological and hydrological controls in a Damköhler number that quantifies the relative effect of Fe(II)-bearing minerals abundance and transport velocity. Analytical solution are validated using reactive transport simulations with CrunchFlow. We use this framework to interpret field data in two critical zone observatories with contrasted chemical properties.

2 Reactive transport of dissolved oxygen and iron

2.1 Model conceptualisation

To unravel the respective roles of hydrological and geological controls on DO and Fe^{2+}, we consider a travel time formulation (Maher, 2010). For a given flowpath, we model a reaction in parcel of transported fluid as a kinetic system controlled by the travel time (Fig. 1). We quantify interactions between oxic recharge water and Fe(II)-bearing minerals and derive approximate analytical expression of both DO and Fe^{2+} as a function of fluid travel time. We assume that the flowpath cross a shallow regolith zone followed by an unweathered zone in which DO reacts with Fe^{2+} produced from minerals dissolution (Figure 1). We neglect here the transport time in the non-reactive regolith, which we assume to be short compared to the travel time in the non-weathered zone. Furthermore, we do not resolve explicitly the fracture-matrix exchanges and consider an effective travel time which represents effectively the time during which the fluid is in contact with reactive elements. In a second step, we relate time to depth using and average transport velocity and derive equations for the evolution with depth of DO and Fe^{2+}.

Table 1. Glossary of main variables in the text

Nomenclature	Units	Variable
a	$[mol.kg_w^{-1}]$	Activity
C	$[mol.kg_w^{-1}]$	Concentration
Da		Damköhler number
DO		Dissolved Oxygen
E_a	$[kcal.mol^{-1}]$	Activation energy
Fe^{2+}		Dissolved Fe(II)
$Fe-clay$		Fe-rich clay (secondary mineral)
Φ	[-]	Volume fraction
γ	$[mol_{Fe}.kg_w^{-1}.s]$	Reducing capacity of mineral species
Γ	[-]	Q for all ionic species in mineral excepting iron
Q	[-]	Ionic Activity Product
j		Index standing for b: biotite, c: Fe-clay, d: dissolving mineral, p: precipitating mineral
K_H	$[mol.atm^{-1}.kg_w^{-1}]$	Henry's constant
K_{sp}	[-]	Solubility product for mineral
K_w	$[mol^2.L^{-2}]$	Auto-dissociation constant of water
k	$[mol.m^{-2}.s^{-1}]$	Kinetic constant for mineral dissolution
k_{ox}	$[kg_w.mol^{-1}.s^{-1}]$	Kinetic constant for iron oxidation by DO
Λ	[-]	Lithological parameter
ν	[-]	number of Fe^{2+} atoms per mineral formula
R	$[mol.s^{-1}]$	Reaction rate
s	$[mol.L^-1]$	Mineral solubility
S_M	$[m^2.g^{-1}]$	Specific surface area
S_V	$[m^2.m^{-3}]$	Bulk surface area
t	$[y]$	Mean fluid travel time
τ_c	$[y]$	Characteristic time for DO consumption
τ_t	$[y]$	Characteristic time for DO transport
$\overline{v_a}$	$[m.y^{-1}]$	Apparent vertical velocity
ω	[-]	Porosity
z_c	$[m]$	Reference depth for DO transport

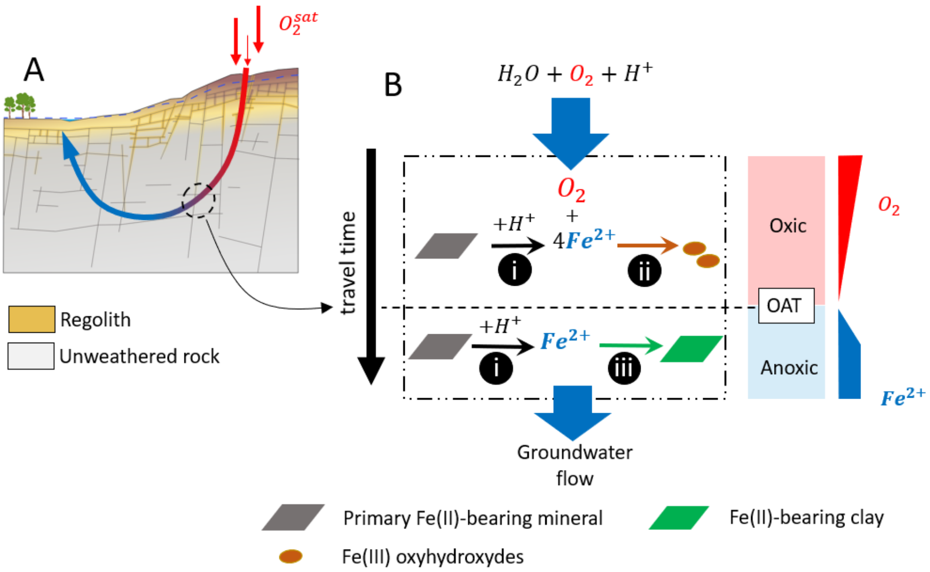

Figure 1. Conceptual model for the transport and reactivity of DO and Fe^{2+} along a flow-path (A). (B) In the unweathered rock, DO is consumed owing to the following reaction network i) Fe(II)-bearing minerals dissolution, promoted by groundwater acidity, releases Fe^{2+} ii) aqueous oxidation of dissolved iron by DO and precipitation of Fe(III) oxyhydroxydes iii) incongruent mineral dissolution releases Fe^{2+} and forms Fe(II)-bearing clay. OAT indicates the Oxic-Anoxic Transition along the pathway.

2.2 Geochemical system

We study the coupling between two geochemical reactions: the dissolution of iron-bearing minerals to produce dissolved iron (Fe^{2+}) and its reaction with dissolved oxygen transported from recharge fluids (Fig. 1). Similarly to previous works (Sidborn & Neretnieks, 2008; Macquarrie et al., 2010), we assume that Fe(II)-bearing minerals dissolve through a non-oxidative mechanism that liberates Fe^{2+} while consuming acidity, and that Fe(II)-bearing clays (Fe-clay) precipitate.

We model the dissolution and precipitation kinetics for mineral reactions using the Transition State Theory (TST), expressing the reaction rate for a mineral j (R_j) as (Lasaga, 1984) :

$$R_j = S_{V,j} \Phi_j \omega^{-1} \left(k_{j,H} a_H^{n_H} + k_j + k_{j,OH} a_{OH}^{n_{OH}} \right) e^{-\frac{E_{a,j}}{RT}} \left(1 - \frac{Q_j}{K_{sp,j}} \right), \quad (1)$$

With $S_{V,j}$ $[m^2.m^{-3}]$ the Specific Surface Area per volume, $(k_{j,H}, k_j, k_{j,OH})$ $[mol.m^{-2}.s^{-1}]$ the intrinsic reaction constants at 25 $°C$ at acid, neutral and basic pH, respectively; a the activity and n the affinity factor of the indicated ion accounting for reaction catalysis by pH, $E_{a,j}$ the activation energy, Q_i the activity product and $K_{sp,j}$ the solubility product for mineral species j, ω is the fracture porosity, R is the ideal gas constant and T the absolute temperature.

The aqueous reaction between dissolved oxygen and dissolved iron, and the corresponding kinetic law, are respectively:

$$4Fe^{2+} + O_2 + 4H^+ \rightarrow 4Fe^{3+} + 2H_2O \quad (2)$$

$$R_{ox} = k_{ox} C_{Fe^{2+}} P_{O_2} C^2_{OH^-} \;\; for\; pH > 4.5, \tag{3}$$

with R_{ox} the rate of Fe^{2+} oxidation, k_{ox} the intrinsic reaction constant of oxidation ($1.3{\times}10^{12}\ M^{-2} atm^{-1} s^{-1}$), C_i the concentration of species i in $[mol\ L^{-1}]$ and P_{O_2} the partial pressure of oxygen in [atm] (Singer & Stumm, 1970).

Since groundwater in crystalline rocks is commonly sligthly acid to near-neutral (DeSimone et al., 2014), pH is here buffered at 7, Equations 1 and 2 reduce to:

$$R_j = S_{V,j} \Phi_j k_j^{'} \omega^{-1} \left(1 - \frac{Q_j}{K_{sp,j}}\right), \qquad \text{with } k_j^{'} = k_j|^{25^\circ C} e^{-\frac{E_{a,j}}{R^G\ T}} \tag{4}$$

and

$$R_{ox} = k^*_{ox} C_{Fe^{2+}} C_{O_2}\ , \qquad \text{with } k^*_{ox} = \frac{k_{ox}}{K_H} C^2_{OH^-} \tag{5}$$

2.3 Analytical model

At any time, the change on dissolved oxygen and dissolved iron concentration is the result of the iron release from Fe(II)-bearing minerals dissolution R_d, and iron retention processes, resulting from Fe^{2+} oxidation R_{ox} and precipitation of clay, R_p:

$$\begin{cases} \frac{dC_{Fe^{2+}}}{dt} = \nu_d R_d - \nu_p R_p - R_{ox} \\ \frac{dC_{DO}}{dt} = -\frac{1}{4} R_{ox} \end{cases} \tag{6}$$

where ν_d and ν_p correspond to stoichiometric coefficients accounting for the number of Fe^{2+} per mineral formula in the dissolving or precipitating minerals respectively. R_d and R_p are described by Equation 4 and R_{ox} by Equation 5. In order to solve the system of equations 6, we consider two regimes: i) initially oxic conditions, ii) anoxic conditions once oxygen has been depleted.

2.3.1 Oxic regime

At short travel times, DO is in excess with respect to Fe^{2+} and pH is close to neutrality. Under this condition, very little iron can persist in solution as it is rapidly oxidized according to Equation 2, which has a large kinetic constant. Considering that primary minerals are more abundant than secondary minerals in unweathered rocks, we assume that $R_p << R_d$. Therefore, equation 6 simplifies to:

$$\begin{cases} \frac{dC_{Fe^{2+}}}{dt} + R_{ox} = \nu_d R_d \\ \frac{dC_{DO}}{dt} = -\frac{1}{4} R_{ox} \end{cases} \tag{7}$$

As Fe(II)-bearing minerals are highly under-saturated, the saturation state of the mineral ($\frac{Q_j}{K_{sp,j}}$) tends to zero in Equation 4. Rearranging equation 7 with this assumption yields :

$$\frac{dC_{Fe^{2+}}}{dt} - 4\frac{dC_{DO}}{dt} = \nu_d S_{V,d} \Phi_d k_d^{'} \omega^{-1}. \tag{8}$$

Because DO is in excess, $C_{Fe^{2+}} << C_{DO}$ and thus $\frac{dC_{Fe^{2+}}}{dt} << \frac{dC_{DO}}{dt}$,

which leads to

$$\frac{dC_{DO}}{dt} = -\frac{1}{4} \nu_d S_{V,d} \Phi_d k_d^{'} \omega^{-1}. \tag{9}$$

Hence, the decay of oxygen is controlled by the amount of dissolved iron produced from mineral dissolution. We define the reducing capacity of a mineral j (γ_j) as the flux of iron produced by mineral reaction per unit of volume of fluid:

$$\gamma_j = \nu_j S_{V,j} \Phi_j k_j^{'} \omega^{-1}, \tag{10}$$

By integration, considering the reducing capacity (γ_d) constant, the evolution of DO concentration with the fluid travel time t is expressed by:

$$C_{DO} = C_{DO}(0)\left(1 - \frac{t}{\tau_c}\right), \forall\ t < \tau_c, \tag{11}$$

where τ_c is the characteristic time required to consume DO and reach anoxic conditions,

$$\tau_c = \frac{4C_{DO}(0)}{\gamma_d} \tag{12}$$

The concentration of dissolved iron $C_{Fe^{2+}}$ respects the kinetic law of Equation 5:

$$\frac{dC_{DO}}{dt} = -\frac{1}{4} k_{ox}^* C_{Fe^{2+}} C_{DO}. \tag{13}$$

Hence,

$$C_{Fe^{2+}} = -\frac{4}{k_{ox}^* C_{DO}} \frac{dC_{DO}}{dt}. \tag{14}$$

Inserting equations 11 and 9 into the above expression leads to the evolution of iron concentration as a function of travel time in the oxic regime,

$$C_{Fe^{2+}} = \frac{4}{k_{ox}^*}\left(\frac{1}{\tau_c - t}\right), \forall\ t < \tau_c \tag{15}$$

This analytical model thus yields the following solutions for the coupled evolution of DO and Fe^{2+} for the oxic regime.

$$\begin{cases} C_{DO} = C_{DO}(0)\left(1 - \frac{t}{\tau_c}\right) \\ C_{Fe^{2+}} = \frac{4}{k_{ox}^*}\left(\frac{1}{\tau_c - t}\right), \forall\ t < \tau_c \end{cases} \tag{16}$$

We introduce the non-dimensional Damköhler number Da (Maher, 2010) as the ratio of the characteristic timescale for DO transport τ_t over the timescale for oxygen consumption τ_c (Equation 12):

$$Da = \frac{\tau_t}{\tau_c}. \tag{17}$$

with τ_t the characteristic time for DO transport up to a reference depth z_c while flowing at an apparent vertical velocity $\overline{v_a}$:

$$\tau_t = \frac{z_c}{\overline{v_a}}. \tag{18}$$

Da is thus proportional to the ratio of the reducing capacity (γ) to the apparent vertical velocity ($\overline{v_a}$) :

$$Da = \frac{\gamma}{\overline{v_a}} \times \frac{z_c}{4C_{DO}(0)}. \tag{19}$$

The system of equations for DO and Fe^{2+} can be expressed in terms of the Damköhler regime, such as :

$$\begin{cases} C_{DO} = C_{DO}(0)\left(1 - Da\frac{t}{\tau_t}\right), \forall\ t < \tau_c \\ C_{Fe^{2+}} = \frac{4Da}{k_{ox}^*}\left(\frac{1}{\tau_t - Da\ t}\right), \forall\ t < \tau_c \end{cases} \tag{20}$$

For $Da > 1$, the timescale of DO transport τ_t is longer than the timescale of DO consumption τ_c. Thus, DO supply is transport-limited and the conditions transition from oxic to anoxic along flow paths. Conversely, for $Da < 1$ the timescale of DO consumption is longer than transport. In this case, DO is not depleted because transport overcomes DO consumption and the system remains oxic.

2.3.2 Anoxic regime

Once the available DO has been depleted, the concentration of Fe^{2+} is no longer limited by oxidation (R_{ox} becomes negligible) and then Equation 6 reduces to:

$$\begin{cases} C_{DO} = 0 \\ \frac{dC_{Fe^{2+}}}{dt} = \nu_d R_d - \nu_p R_p \end{cases} \tag{21}$$

Since the dissolution rate of primary silicates is lower than the precipitation rate of secondary phases (Helgeson et al., 1969), we assume that under reducing conditions, the dissolving Fe(II)-bearing mineral is still highly under-saturated ($\frac{Q_d}{K_{sp,d}} << 1$) while Fe(II)-bearing clay (Fe-clay) precipitates ($\frac{Q_p}{K_{sp,p}} >> 1$). Thus, Fe^{2+} is released from the dissolution of primary mineral and part of it precipitates in secondary minerals. According to the definition of R_j (Equation 4) and considering the above approximations for $\frac{Q_j}{K_{sp,j}}$, Equation 21 simplifies to:

$$\frac{dC_{Fe^{2+}}}{dt} = \gamma_d - \gamma_p \frac{Q_p}{K_{sp,p}}, \tag{22}$$

with γ_d and γ_p the reducing capacity, as defined by Equation 10, of respectively the dissolving Fe(II)-bearing primary mineral and the precipitating Fe-clay.

For a general composition of the mineral Fe-clay, the corresponding solubility reaction may be written as:

$$Fe_{\nu_c} Mg_a Al_b Si_c O_{10}(OH)_{m_1} + nH^+ \xrightarrow{K_{sp,p}} \nu_c Fe^{2+} + aMg^{2+} + bAl^{3+} + cSiO_2^c + m_2 H_2O \tag{23}$$

Assuming that activity coefficients are close to 1, the ionic activity product (Q) for the above reaction can be defined as follows:

$$Q_p = \frac{C_{Mg}^a C_{Al}^b C_{SiO_2}^c}{C_H^n} C_{Fe^{2+}}^{\nu_p} = \Gamma_p C_{Fe^{2+}}^{\nu_p}, \tag{24}$$

where C_i is the concentration of species i and Γ_p the concentration product $\forall i \neq Fe^{2+}$ among the elements present in the Fe-clay mineral. The solubility product ($K_{sp,p}$) may be reformulated in an analogous way:

$$K_{sp,p} = \frac{(a\ s_p)^a (b\ s_p)^b (c\ s_p)^c}{10^{-n\ pH}} (\nu_c\ s_p)^{\nu_p} = \Gamma_p^s s_p^{\nu_p}, \tag{25}$$

where s_p is the solubility of Fe-clay and Γ_p^s is the solubility product $\forall i \neq Fe^{2+}$. Replacing the expressions for Q_p and $K_{sp,p}$ in Equation 22 and rearranging gives:

$$-\frac{\Lambda}{\gamma_d} \frac{dC_{Fe^{2+}}}{dt} = \left(\frac{C_{Fe^{2+}}}{s_p} \right)^{\nu_p} - \Lambda\,, \tag{26}$$

with the non-dimensional lithological parameter

$$\Lambda = \frac{\gamma_d \Gamma_p^s}{\gamma_p \Gamma_p} \tag{27}$$

which quantifies the relative reducing capacity between primary to secondary Fe(II)-bearing minerals (γ_d/γ_p) and the deviation from chemical equilibrium (Γ_p^s/Γ_p).

The solution of the differential equation 26 depends on the stoichiometric coefficient for iron per mineral formula of Fe(II)-bearing clay (ν_p). Here, we assume $\nu_p = 2$, which characterizes a typical Fe(II)-rich clay composition according to Sugimori et al. (2008). Solving Equation (26) leads to following solutions under anoxic conditions:

$$\begin{cases} C_{DO} = 0 \\ C_{Fe^{2+}} = s_p \sqrt{\Lambda}\ \tanh\left(\frac{\gamma_d}{s_p \sqrt{\Lambda}}\ t \right). \end{cases} \tag{28}$$

For $t > \frac{s_p\sqrt{\Lambda}}{\gamma_d}$, the transient term in Equation 28 tends to 1 and a pseudo-equilibrium concentration of dissolved iron is reached and expressed by :

$$C_{Fe^{2+}} \to s_p\sqrt{\Lambda} \tag{29}$$

Under anoxic conditions the pseudo-equilibrium concentration of dissolved iron is independent of time and is only driverled by geological factors, here synthesized through the lithological parameter Λ and the solubility of Fe-clay s_p.

2.4 Reactive transport simulations

2.4.1 Base Case Simulation

To test the validity of the approximate analytical expressions derived above, we perform reactive transport simulations using the code CrunchFlow (Steefel & Maher, 2009). We simulate the evolution of dissolved oxygen and Fe^{2+}, as a result of reactions between an oxic water typical of recharge water and a crystalline rock lithology containing quartz, feldspars, biotite and muscovite, with an initial porosity ϕ of 1 (Belghoul, 2010) (see compositions in Suppl. Inf.). In unweathered crystalline rocks, biotite is an ubiquitous Fe(II)-bearing mineral present in high proportions (Bazilevskaya et al., 2013; Holbrook et al., 2019; Hampl et al., 2021; Kim et al., 2017).

Precipitation and dissolution of secondary minerals are allowed to simulate incongruent dissolution of silicate phases. The incongruent dissolution of feldspars is simulated with the formation of kaolinite (Figure 2). Biotite weathering is commonly described as an incongruent dissolution process in which the hydration and progressive replacement of inter-layer cations (i.e. K^+) forms a wide range of Fe-bearing clays (Fe-clay) and Fe(III) oxyhydroxides depending on the leaching and redox conditions (Acker & Bricker, 1992; Scott & Amonette, 1985; Sequeira Braga et al., 2002; Murakami et al., 2003; Dideriksen et al., 2010; Hampl et al., 2021). In the present simulations, we consider the precipitation of goethite as a typical Fe-oxyhydroxyde found in oxic weathering fronts (Dideriksen et al., 2010) (Figure 2). For anoxic conditions, Sugimori et al. (2008) have documented that Fe-rich corrensite forms as the dominant secondary phase. However, because thermodynamic and kinetic parameters for corrensite are poorly known, for our simulations we allow the formation of chlorite since this mineral has a similar stability field and paragenetic relationships with corrensite (Beaufort et al., 1997) (Figure 2).

Figure 2 presents the evolution of DO, Fe^{2+} concentrations in the aqueous phase and mineral saturation indexes simulated with the numerical model as a function of the mean fluid travel time, over a period of 750 years. DO decreases linearly until it gets depleted and a non-linear transition from oxic to anoxic conditions is observed. The evolution of the saturation indexes (SI) of mineral species with the mean fluid travel time (Figures 2-B and 2-C) indicates that iron is being released from biotite during both oxic and anoxic conditions ($SI_{biotite} < 0$ indicates dissolution). Under oxic conditions, the Fe^{2+} concentration is driven by the presence of DO and its oxidation into Goethite ($SI_{goethite} > 0$ indicates precipitation). On the other hand, when $t > \tau_c$, the Fe^{2+} concentration is driven by the precipitation of Fe(II)-bearing clay as indicated by the change on $SI_{chlorite}$ from undersaturated (oxic conditions) to saturated (anoxic conditions) conditions.

2.4.2 Validation of analytical expressions

We compare numerical simulations with analytical solutions derived for the evolution of both DO and Fe^{2+} concentrations under oxic (Equation 16) and anoxic (Equation 28) conditions. Thermodynamic parameters from Table 2 and mineral compositions are used to calculate the parameters of the analytical solutions. The analytical expressions for both DO and Fe^{2+} accurately capture the numerical simulations and the predicted characteristic time τ_c (Equation 12) coincides with the non-linear oxic-anoxic tran-

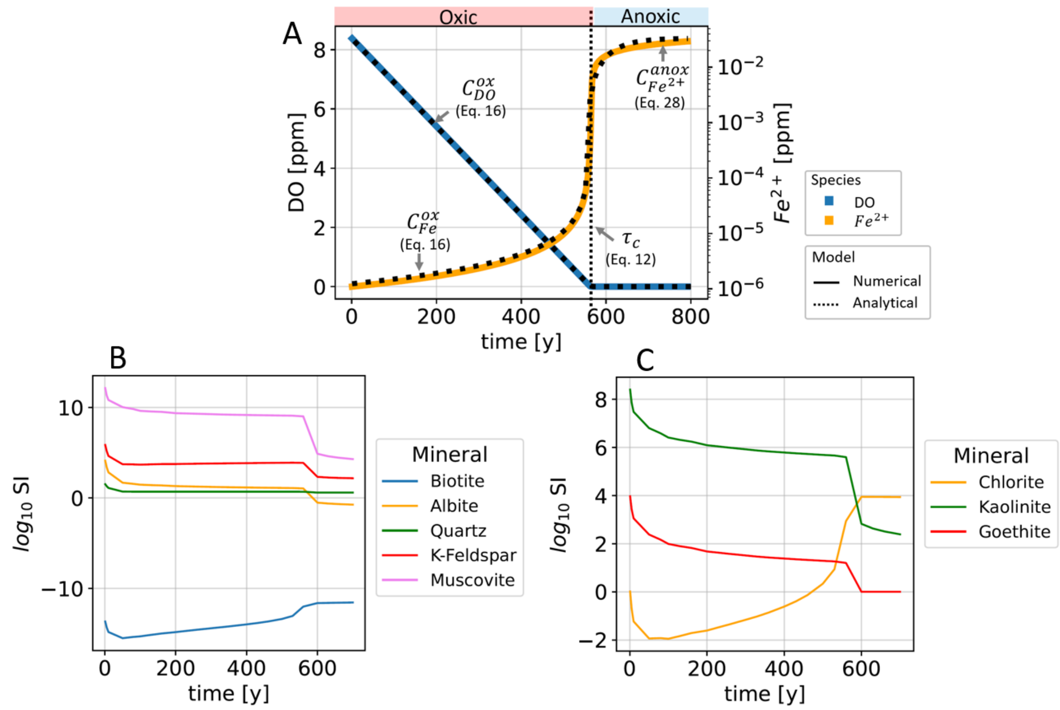

Figure 2. Simulation results for the Base Case scenario, obtained with Crunchflow for a lithological composition with $\gamma_d = 2 \times 10^{-3} mol.m_w^{-3}.y^{-1}$, $\Lambda = 20$. (A) Evolution of dissolved oxygen and iron concentration as a function of travel time. C_{DO}^{ox} and C_{Fe}^{ox} correspond to concentrations under oxic conditions, whereas C_{DO}^{anox} and C_{Fe}^{anox} represent concentrations at anoxic conditions. τ_c is the characteristic time for DO depletion. (B) and (C) represent the evolution of saturation Indexes (SI) as a function of fluid travel times for primary and secondary minerals, respectively.

sition from the numerical model, which validates the assumptions made to derive the analytical solutions.

To further evaluate the validity of the analytical approximations, a sensitivity analysis is carried out by varying the main parameters identified from the analytical solutions. With the numerical model and the analytical solutions 16, we evaluate i) the influence of the reducing capacity (Eq. 10) and of the mean fluid travel time on DO and Fe^{2+} concentrations (Figure 3-A and B) in the oxic regime ; ii) the influence of the reducing capacity of biotite on the characteristic time for oxygen consumption τ_c (Figure 3-C) ; iii) the influence of clay precipitation capacity on the equilibrium concentration of Fe^{2+} (Figure 3-D). The sensitivity on the reducing capacity of biotite is tested by varying the specific surface area S_M over 4 orders of magnitude and the fraction of biotite in the rock Φ_d by a factor 20. The sensitivity on the clay precipitation capacity is tested by varying the specific surface area S_M over 3 orders of magnitude and the initial fraction of clay in the rock Φ_p over 4 orders of magnitude.

The approximated analytical solutions are in good agreement with the simulations for the full range of tested parameters and simulation times. The equilibrium Fe^{2+} concentrations calculated with the analytical solutions are slightly lower than the numerical simulations at low initial fraction of clay in the rock. This is due to the fact that the fraction of clay is recalculated at each time step in the numerical model while assumed constant in the analytical solution, and the change in clay fraction with time can be significant at very low initial clay fractions.

Table 2. Geochemical parameters used in the numerical modelling and to calculate non-dimensional numbers in the analytical solutions. References in column *Source* correspond to (1): (Robie A. & Philip M., 1962), (2): (Malmstrom et al., 1995), (3): (Palandri & Kharaka, 2004), (4): (Singer & Stumm, 1970)

Parameter		Value		Source
		biotite[a]	Fe-clay[b]	
Molar volume $[cm^3.mol^{-1}]$	V_m	149.65	215.88	(1)
Molecular weight $[g.mol^{-1}]$	MW	417.3	713.5	
Solubility product [-]	K_{sp}	$10^{41.1}$	$10^{47.6}$	(2)
Solubility $[mol.L^{-1}]$	s	$10^{-3.49}$	$10^{-6.85}$	
Activation energy $[kcal.mol^{-1}]$	E_a	5.26	21.03	(3)
kinetic dissolution constant $[mol.m^{-2}.s^{-1}]$	k_d	$10^{-12.55}$	$10^{-12.52}$	(3)
Aqueous parameters				
kinetic oxidation constant $[L^2.mol^{-2}.atm^{-1}.s^{-1}]$	k_{ox}	$10^{12.12}$		(4)
Initial DO concentration $[mol.kg_w^{-1}]$	$C_{DO}(0)$	2.62×10^{-4}		
Henry's constant for O_2 $[mol.atm^{-1}.L^{-1}]$	K_H	$10^{-2.89}$		
Water auto-dissociation constant $[mol^2.L^{-2}]$	K_w	10^{-14}		
pH		7.0		

[a]: values for phlogopite
[b]: based on properties for chlorite

As expected, less oxic conditions occur in systems with higher biotite contents (Figures 3-A and B). Insets in figures 3-A and B show that longer mean fluid travel times can counterbalance low reducing capacity (low biotite content and/or low S_M), leading to more persistent oxic conditions. This interplay between the reducing capacity and travel time is captured by the characteristic time for oxygen consumption τ_c (Equation 12) in agreement with simulations (Figure 3-C). The characteristic time for oxygen consumption decreases with the reducing capacity (both with the biotite content and S_M), leading to a longer persistence of oxic conditions in low reducing capacity rocks. The equilibrium Fe^{2+} concentration decreases with increasing clay precipitation capacity (initial Fe(II)-clay content and S_M), showing that Fe^{2+} remains dissolved if it can not precipitate into clays.

2.5 Hydrological and geological drivers for DO and Fe^{2+} concentrations

While the numerical model allows for a complex and realistic reactive modeling framework, the analytical solutions provide a framework to understand and quantify the hydrological and geological drivers for the evolution of DO and Fe^{2+} in crystalline rocks (Figure 4).

The dissolved oxygen concentration predicted by Equation 20 is represented as a function of the fluid travel time and the reducing capacity, the two main parameters expressing the hydrological and geological controls in the Damköhler number (Figure 4). The counteracting effects of fluid travel time and reducing capacity imply that there is a fundamental indeterminacy on the hydrological and geological drivers when considering oxygen alone. A given concentration of oxygen can be obtained by a range of different combinations of hydrological and geological parameters. In rocks with low reducing capacities, DO concentrations are poorly sensitive to travel time since DO consumption is very slow ($Da < 1$). For high reducing capacity values, DO concentrations evolve rapidly with travel time due to fast reaction kinetics ($Da > 1$).

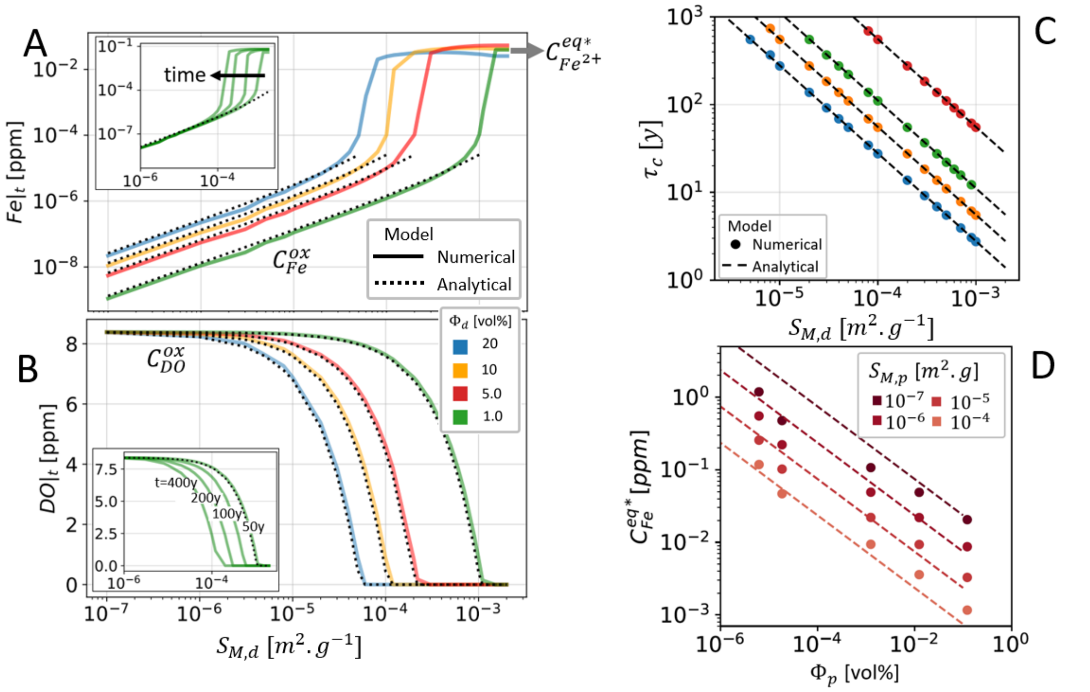

Figure 3. Sensitivity analysis for the numerical and analytical models. Subfigures (A) and (B) present concentration profiles vs S_M for DO and Fe^{2+}, respectively. Main plots are sensitivities to Φ_d at t = 50y while inserts show the evolution with time for the $\Phi_d = 1\%$ case. Analytical solutions come from equations 16 and 28. Subfigure (C) presents the sensitivity of τ_c to the reducing capacity (Equation 12). Subfigure (D) presents the sensitivity of the equilibrium Fe^{2+} concentration to the clay precipitation capacity. Subscript d stands for dissolving mineral (e.g. biotite) and subscript p stands for precipitating mineral (e.g. Fe-clay).

When oxygen is depleted, Fe^{2+} concentrations tend toward the pseudo-equilibrium concentration (Equation 29), which is controlled by the relative abundance of primary and secondary Fe(II)-bearing minerals expressed through the non-dimensional number Λ(Equation 27). As a consequence, Fe^{2+} concentrations under anoxic conditions are mainly driven by the geological context of the subsurface. Therefore, the joint analysis of both DO and Fe^{2+} concentrations gives independent constrains on the potential roles of hydrological and geological processes on the distribution of oxygen in the subsurface, which we discuss using field data in the following section.

3 Field study at the Ploemeur CZO (France)

To evaluate the modelling framework presented above, we test it against extensive field observations of DO and Fe^{2+} concentrations in the subsurface available at the Critical Zone Observatory of Ploemeur (France). The Ploemeur CZO includes two subcatchments located at a distance of about 4 km: the Kermadoye site and the Guidel site. Both catchments are characterized by a fractured bedrock with similar lithologies and an oceanic climate but differ significantly in their DO and Fe^{2+} concentrations. It is thus well suited to test the concepts presented above.

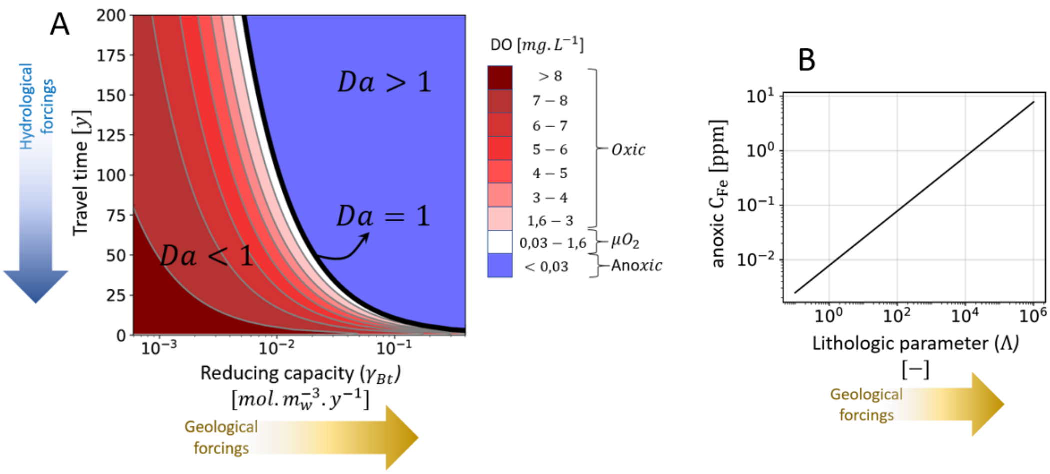

Figure 4. (A) Dependence of DO concentrations to geological (x-axis) and hydrological (y-axis) forcings. Multiple combinations of reducing capacity and travel time can result in a same prediction of DO concentration (e.g. iso-concentration lines for C_{DO}). Stronger geological forcings (higher reducing capacity of a certain lithology as in Equation 10) limit the persistence of DO to very short travel times (favor anoxic conditions) and vice versa. Higher hydrological forcings in y-axis (faster groundwater velocities) favor deeper transport of DO for a same travel time (Equation 30). (B) Dependence of iron concentrations to the lithological parameter (Λ) at anoxic conditions. The lithological parameter is defined in Equation 26

.

3.1 Site presentation

The Ploemeur Critical Zone Observatory (CZO) belongs to the H+ hydrogeological network (`http://hplus.ore.fr/en/`), the French network of critical zone observatories OZCAR (`https://www.ozcar-ri.org/fr/` and the e-LTER european infrastructure (`https://deims.org/731f3ced-148d-4eb5-aa46-870fa22be713`). It is located in the southern part of the Armorican massif in Brittany, France. The region is characterized by the intersection of two main tectonic features : (1) a gently dipping (around 30º to the north) contact zone between a Late Hercynian granite and the surrounding micaschist rock, (Touchard, 1999); and (2) a dextral-slip normal fault zone which strike Nord 20º and dip East 70º (Ruelleu et al., 2010). Both are the main transmissive structures of the fractured-bedrock aquifer, characterized by a relatively large average transmissivity on the order of $10^{-3} m^2/s$ sustained by a well connected fracture network (Le Borgne et al., 2007; Jiménez-Martínez et al., 2013)

The Kermadoye aquifer has been exploited for drinkable water supply since 1991 at an average pumping rate of 1 $Mm^3.yr^{-1}$. This particularly high production rate is attributed to the presence of the regional contact zone which drains flows towards the vertical faults (Leray et al., 2013; Jiménez-Martínez et al., 2013; Roques et al., 2016). The Kermadoye catchment is monitored with 22 boreholes, with depths ranging from 50 to 150 meters. The majority of them cross the contact zone between micaschist and granite or are entirely in the granite. The Guidel catchment is not pumped, although it has similar hydraulic properties as the Kermadoye catchment. Natural groundwater flows converge to supply a stream and a wetland. The Guidel catchment is located North of the contact zone (see Figure 5)and is monitored by 25 boreholes of depths ranging from 50 to 150 meters since 2009. These boreholes intersect mostly micaschists. Recent studies have shown that the mixing of oxygen rich and iron rich fluids at fracture intersections or in the wetland, sustains microbial hotspots, dominated by iron-oxidizing bacteria (FeOB) (Bethencourt et al., 2020; Bochet et al., 2020). Understanding and modelling DO and Fe^{2+} concentrations at this site is thus of particular interest.

The comparison of the two sites is particularly interesting as the hydrological forcing is stronger at the Kermadoye site due to pumping. Furthermore, while the two sites have comparable geology, the contact zone is deeper at Guidel site, which may be more influenced by the micaschist lithology. Since the two sites have contrasted DO and Fe^{2+} signatures, they are particularly relevant test grounds to resolve the hydrological and geological controls on these chemical properties.

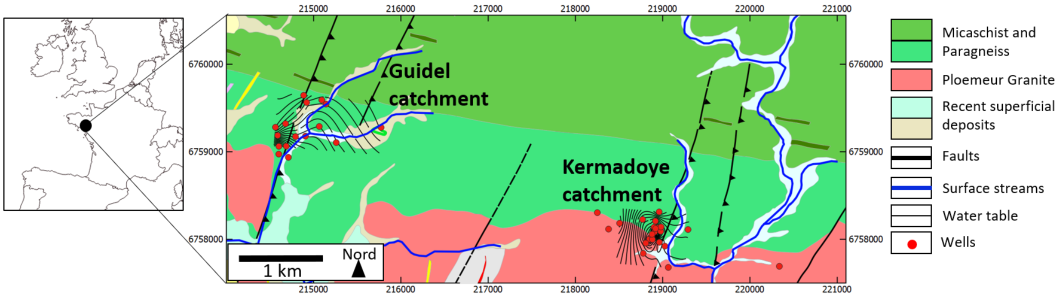

Figure 5. Geographical location, geological and hydrogeolocical maps of the Ploemeur Critical Zone Observatory and its two catchments, Guidel and Kermadoye. The geological map is reproduced from (Béchennec et al., 2012a)

Table 3. General characteristics of the study site

	Guidel	Ploemeur
Generalities		
Lat. Long.	47º45'16"N 3º28'51"W	47º44'50"N 3º25'38"W
Mean Altitude (m.a.s.l.)	15.1	26.7
Groundwater flow-regime	Natural circulation	Pumped since 1991
Geology		
Dominant bedrock lithology	Mica-schist, Paragneiss	Granite
Age	Ordovician inf	Carboniferous
Mean [min, max] depth to fresh bedrock (m)	17 [4, 34]	30 [10, 44]
Climate		
Climate type	Oceanic	
Mean annual rainfall (mm)	924[a]	
Mean annual temperature (ºC)	12.1[a]	
Mean Altitude (m.a.s.l.)	15.1	26.7

[a]: data from Lann-Bihoué weather station, averaged from the period 2006 - 2014

3.2 DO and Fe^{2+} depth profiles

The DO and iron concentrations measured in the two catchments are represented as a function of depth in Figure 6. Each point represents the concentration measured in front of the main transmissive fracture in each borehole (see Supplementary information for DO and Fe^{2+} measurement methods). Since there are locally rapid vertical flows around boreholes, we converted the fracture depth to an effective depth representative of larger scale flow path using the temperature anomalies measured in boreholes (see Suppl. inf.). DO concentrations decrease with depth, from values close to saturation down to values close to the detection limit (0.1 $mg.L^{-1}$). Both catchments reach the oxic-anoxic transition, but at significantly different depths. The oxic-anoxic transition takes place between 100 and 150 m depth at the Guidel site. At the Kermadoye site it takes place between 200 to 400 m depth. The decrease in DO is associated with an opposite gradient of Fe^{2+} (see Figure 6-B). Fe^{2+} concentrations in Guidel increase up to an average value of 2.8 ± 1.7 ppm, while in Kermadoye, Fe^{2+} concentrations increase up to $6.3\times 10^{-2} \pm 2.7\times 10^{-2}$ ppm, i.e. about two orders of magnitude lower than in Guidel.

3.3 Model application to field data

In order to investigate the depth-distribution of DO and Fe^{2+}, we transform the mean fluid travel time into depth (z) by considering an apparent vertical velocity ($\overline{v_a}$), such as:

$$t = \frac{z}{\overline{v_a}} \tag{30}$$

Thus, the system of equations can be expressed as a function of depth:

$$oxic : \begin{cases} C_{DO}(z) = C_{DO}(0)\left(1 - Da\frac{z}{z_c}\right) ,\forall\ z < \frac{z_c}{Da} \\ C_{Fe^{2+}}(z) = \frac{4v_a}{k^*_{ox}}\left(\frac{1}{z_c - Da\ z}\right) ,\forall\ z < \frac{z_c}{Da} \end{cases} \tag{31}$$

$$anoxic : \begin{cases} C_{DO}(z) = 0 \\ C_{Fe}(z) = s_c\sqrt{\Lambda}\tanh\left(\frac{4C_{DO}(0)Da}{s_c\sqrt{\Lambda}}\frac{z}{z_c}\right) ,\forall\ z > \frac{z_c}{Da} \end{cases} \tag{32}$$

with z_c the reference depth in Equation 18. Here, we define $z_c = 100$ m, which corresponds to the average depth of our measurements (Figure 6). The dissolved iron concentratio nC_{Fe} only depends on both Da and Λ for $z < \frac{z_c s_c\sqrt{\Lambda}}{4C_{DO}(o)Da}$. At deeper depths, C_{Fe} only depends on the lithological parameter and Equation 32 reduces to the pseudo-equilibrium concentration (Equation 29).

3.4 Comparison of field data and model simulations of DO and Fe^{2+}

The analytical solutions for DO and Fe^{2+} for the oxic and anoxic regimes (equations 20 and 29) are fitted to the measured DO and Fe^{2+} depth-profiles at the two sites. Under oxic conditions, the solution for DO has one parameter, the Damköhler number Da, and the solution for Fe^{2+} depends on both Da and on the apparent vertical velocity ($\overline{v_a}$) (Equation 20). Theoretically, the combined resolution of the two equations for DO and Fe^{2+} should allow to fit Da and $\overline{v_a}$, and thus to estimate the reducing capacity of the bedrock (γ).

The analytical solution captures the approximate linear decrease in DO with depth in both catchments (Figure 6). The analytical solution is also compatible with the evolution of Fe^{2+} on both sites. For the Guidel site this evolution is well defined over about three orders of magnitude in concentration. For the Kermadoye site, the maximum concentration data is much smaller and therefore the range of observation is small above the detection limit. Some discrepancies are observed for few Fe^{2+} data points for shallow samples at the two catchments (blue box in Figure 6). This mismatch could be due to reactions of DO or Fe by other reaction pathways, particularly if organic matter is available (Wolthoorn et al., 2004; Serikov et al., 2009; Nordstrom, 2011).

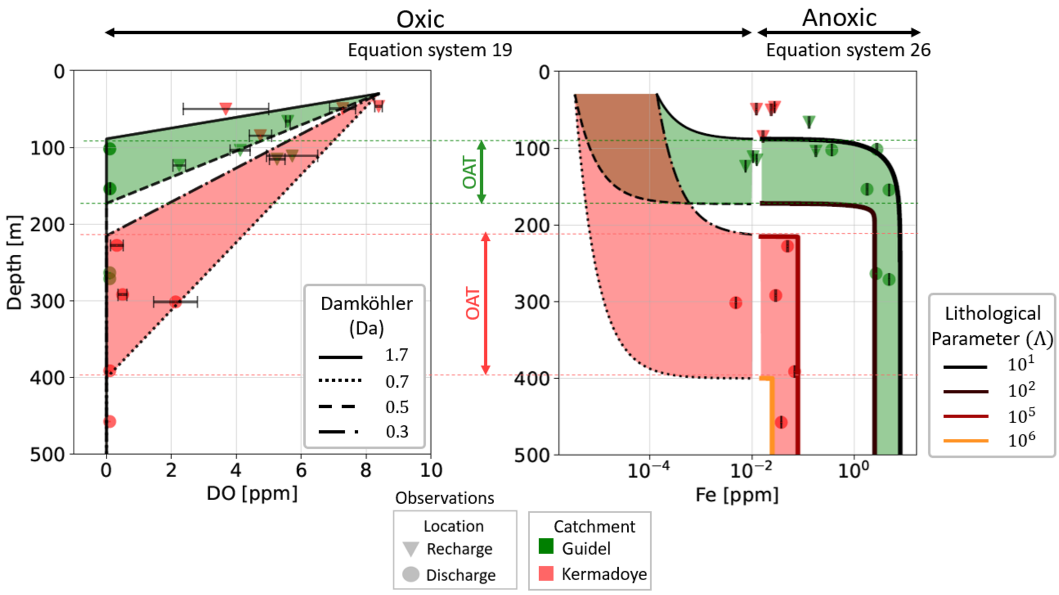

Figure 6. Distribution of DO and Fe^{2+} concentrations as a function of depth for two catchments. Measured field data are represented with dots and triangles, in green for the Guidel site and in red for the Kermadoye site. In the oxic part, analytical solutions are drawn as curves with different values of Da for DO and Fe^{2+} (Equations 20,19). In the anoxic part, analytical solutions for Fe^{2+} are drawn with different values of λ. Sample depth has been inferred using temperature as a proxy. OAT corresponds to the Oxic-Anoxic Transition ranges.

The range of Damköhler numbers can be relatively well constrained as consistent values of Da explain jointly the linear decrease of DO and the non-linear increase of Fe^{2+}. The Da values range between 0.7 and 1.7 at the Guidel site and between 0.3 and 0.5 at the Kermadoye site (Figure 6). On the other hand, the value of $\overline{v_a}$ influences the very low concentrations of Fe^{2+} at shallow depths (see Suppl. info.), for which Fe^{2+} concentrations are below detection limits and therefore $\overline{v_a}$ can not be constrained directly from these data. Under anoxic conditions, the pseudo-equilibrium concentration in Fe^{2+} only depends on the lithological properties (Equations 29). The parameter Λ is relatively well constrained since the maximum Fe^{2+} is very different between the two sites: Λ ranges between 10^1 and 10^2 for the Guidel site, and between 10^5 and 10^6 for the Kermadoye site (Figure 6). The large difference in the two values of Λ suggests that the contrast of the main lithological properties of the two sites is likely more important than possible differences in hydrological properties.

Therefore, the analysis of DO and Fe^{2+} concentration data under oxic conditions provides a good constrain on the Damköhler number, suggesting that the Guidel catchment is more reaction-limited than the Kermadoye catchment.However, this still leaves an uncertainty on whether this difference may be explained by a hydrological or geological contrast. An additional constrain is given when analyzing Fe^{2+} concentrations in the anoxic regime, suggesting an important lithological difference between the two catchments.

4 Discussion

4.1 Discriminating hydrological and geological controls from field data

Despite geographical, climatic and lithological similarities between the two sites, the DO and Fe^{2+} depth-profiles are significantly different. According to our model, this difference may be explained by a factor 3 in the Damköhler numbers Da, the ratio of the transport to reaction time scales, and a factor of 10^4 in the Λ number, which represents geochemical properties such as the reducing capacity of Fe(II)-bearing minerals and the deviation from chemical equilibrium for clay precipitation. The difference in Damköhler numbers can be either due to a contrast in transport velocity or dissolution rates. We discuss these two hypotheses in the following.

We first consider the hypothesis that would attribute DO and Fe^{2+} differences to a contrast in hydrological properties. This may be plausible since the Kermadoye site is pumped while the Guidel site is not. Under this hypothesis, the smaller Da for the Kermadoye site would indicate a factor three increase in average groundwater velocity compared to the Guidel site. However, a geochemical analysis at the Kermadoye site has shown that pumping tends to increase it due to the increase of the contribution of deep groundwater flow paths (Roques et al., 2018). This was confirmed by a hydrogeological model showing an increase in groundwater ages at the pumping well (Leray et al., 2014). Therefore, it is unlikely that flow acceleration due to pumping would explain the factor three contrast in Damköhler number.

We now consider the second hypothesis stating that the difference in Da would result from a 3-fold contrast in the reducing capacity γ_d of the rock. The Guidel site is composed mostly of micaschists, while the Kermadoye site is composed of both micaschists and granites (Figure 5). Mineralogical analyses carried on the two rocks indicate that micaschists contain about 7 times more biotite than granite. Therefore, assuming that about 50% of groundwater flowpaths were interacting with granites and 50 % with micaschists, the average reducing capacity of the Kermadoye aquifer would be around 3 times lower than the reducing capacity of the Guidel site. This hypothesis would therefore explain a difference of 3 in the Da of the two catchments. The difference in the lithology of both catchments is also supported by the large difference in the parameter Λ, that is entirely related to geochemical parameters (Equation 27). The difference of 4 orders of magnitude found on the two sites could be explained by higher inherited contents of clays in granite. Indeed, granites contain higher proportions of plagioclase that are readily weathered into clays (Goldich, 1938), and furthermore supported by the presence of kaolins at the edge of the granite in the site (Béchennec et al., 2012). However, the large difference in Λ could also be related to mineral surface areas which are hard to constrain and vary by orders of magnitude in rocks (Wild et al., 2019; Ackerer et al., 2020).

The analysis of DO and Fe^{2+} data with the presented modelling framework provides key constrains on the hydrological and geological drivers of reactive transport processes. Although the two considered sites are *a priori* very similar in terms of hydrological and geological contexts, our findings suggest that differences in the proportion of granite and micaschist lead to a strong contrast in DO penetration with depth and Fe^{2+} concentrations. Moreover, we provide new constrains on the hydrogeological functioning of the sites. While previous studies suggested that groundwater was recharged and transported through the micaschist and deeper collected at the contact zone between granite and micaschist (Leray et al., 2013) at the Kermadoye site, this analysis suggests here that there is also a significant proportion of groundwater flowing through the granite.

4.2 Controls of DO and iron concentrations in crystalline rocks

The depth of the oxic-anoxic transition in crystalline rocks is controlled by the relative importance of the reducing capacity of the rocks and the effective transport of oxygen from the surface, quantified here by the Damköhler number (Figure 6-A). Linear trends of DO with depth have been observed in other hard-rock systems like the Clara mine in Germany (Bucher et al., 2009) or the Western Canadian Sedimentary Basin (Ruff et al., 2022), such as predicted by our model.

The reducing capacity can be considered as a value inherited from the geology, that varies slowly in time. For instance, Macquarrie et al. (2010) showed a decrease of 0.2 % of biotite content in 2 ky under oxic conditions. On the other hand, groundwater table fluctuations or perturbations of the flow regime (e.g. pumping) can be very rapid (timescales ranging from days to the season (Molenat et al., 1999; Jiménez-Martínez et al., 2013; Guillaumot et al., 2022)). Thus, temporal changes in the oxic-anoxic depth in a particular system are likely mostly due to hydrological fluctuations.

4.3 Persistence of dissolved oxygen in the subsurface

Subsurface environments for which the timescales of DO transport are shorter than timescales of DO consumption (i.e. transport-limited regime, $Da < 1$) favor the deep transport of DO in crystalline rocks, which has a major impact on biogeochemical processes in the critical zone. The occurrence of DO in bedrock is responsible for deep weathering induced fracturing (WIF), Kim et al. (2017), which has been observed in 100 m-deep rock cores (Dideriksen et al., 2010; Bazilevskaya et al., 2013; Antoniellini et al., 2017; Holbrook et al., 2019; Krone et al., 2021; Hampl et al., 2021). By quantifying the dynamics of DO and the parameter controlling the distribution of DO, we provide controls on the conditions favorable for the active oxidative weathering of the deep subsurface. For instance, Bazilevskaya et al. (2013) attributed the thicker regolith in felsic rockes (e.g. granites) compared to mafic rocks (e.g. micaschists) to higher degree of fracturing and higher advective transport of DO with groundwater. We argue that, besides differences in advective transport, the lower reducing capacity of felsic rocks could also explain deeper penetration of DO in the subsurface.

Furthermore, dissolved oxygen exerts a first control on subsurface microbial processes, such as aerobic respiration or denitrification (Dalsgaard et al., 2014; Kolbe et al., 2019) and therefore structures the habitability of subsurface ecosystems. The respiration of Fe-oxidizing bacteria (FeOB) is of particular interest because of the ubiquity of both iron and FeOB (Melton et al., 2014; Kappler et al., 2021) as well as the coupling of the iron cycle with biogeochemical cycles of carbon, sulphur and nitrogen (Casar et al., 2021). The activity of FeOB at near-neutral pH environments requires the simultaneous presence of Fe^{2+} and microaerobic DO concentrations (Druschel et al., 2008; Maisch et al., 2019) while Fe^{2+} and DO often do not coexist because of the rapid oxidation of Fe^{2+}. From observations at the Guidel site, Bochet et al. (2020) suggested that the formation of subsurface FeOB hot-spots is favored by the mixing of oxic recharge water with deep anoxic iron-rich water at fracture intersections. As discussed above, the equilibrium Fe^{2+} concentration (Equation 29) is much lower for granite than for micaschist (Figure 6-B). Therefore, even if oxic and anoxic groundwater mix in granite system, the low dissolved iron concentrations does not favor the formation of FeOB hot-spots because Fe^{2+} is limiting. The depth of formation of subsurface FeOB hot-spots therefore not only depends on the transport of DO but also on the availability of Fe^{2+}, which is function of the geological context.

5 Conclusions

In this study, we developed a modeling framework to describe the depth-distributions of dissolved O_2 and Fe^{2+} concentrations in crystalline rocks, which play a central role in a large range of biogeochemical processes. We derived a set of approximate analytical solutions, validated with reactive transport simulations, that quantify the parameters controlling jointly DO and Fe^{2+} evolution in the subsurface. Under oxic conditions, DO concentrations decrease linearly with fluid travel time following a slope that is function of the reducing capacity of the bedrock. In this regime, dissolved Fe^{2+} remains low because its aqueous oxidation by DO is faster than its release by minerals dissolution. At the Oxic-Anoxic Transition, DO is depleted and Fe^{2+} concentrations show a rapid non-linear increase up to a pseudo-equilibrium concentration that is controlled by the relative abundance of primary to secondary Fe(II)-bearing minerals. These reactive transport dynamics can be understood with two non-dimensional paramers: the Damköhler number Da and the lithological parameter Λ.

We use this framework to interpret DO and Fe^{2+} concentrations measured extensively over two neighboring crystalline catchments with similar hydrogeological properties but contrasted chemical properties. The differences in the depth of the oxic-anoxic transition and in the Fe^{2+} pseudo-equilibrium concentration are successfully modeled and explained by differences in Da and λ. The interpretation of DO alone leads to a fundamental indeterminacy in the respective role of geological and hydrological properties that may explain the difference in Damköhler numbers. However, the joint investigation of DO and Fe^{2+} provides additional constrains, point to the role of a geological contrast, here likely due to a difference in the relative proportion of granite and micaschist in the two sites.

The methodology presented here may be implemented on other sites and contexts, to understand and model the depth of the oxic-anoxic transition. The two non-dimensional numbers can be estimated from field data as a guide for DO transport in the subsurface. Here, we investigated the oxidation of Fe^{2+} by dissolved oxygen and assumed that no other oxidants could oxidize Fe^{2+} after DO depletion. However, the presence of alternative oxidizing agents such as Nitrates or Mn(IV) could promote further iron oxidation under anoxic conditions. In this case, the predicted rise of Fe^{2+} concentrations up to the pseudo-equilibrium concentration ($C^{eq*}_{Fe^{2+}}$) would be shifted deeper until the depletion of all oxidizing species. The derivation of the analytical solutions can also be adapted to other reactions involving dissolved reactants and minerals. While here we considered a simplified approach based on an effective travel time, it would be interesting to investigate the form of the analytical solutions and the corresponding dimensionless parameters when representing explicitly structural heterogeneities and fracture-matrix exchanges.

Acknowledgments

This research was funded, in whole, by ANR EQUIPEX CRITEX project (ANR-11-EQPX-0011) and the ERC project ReactiveFronts (648377). We are very grateful to the french networks of hydrogeological sites H+ (https://hplus.ore.fr/en/) and of critical zone observatories OZCAR (https://www.ozcar-ri.org/) for providing access to the Ploemeur CZO. We also thank the technical services of Geosciences Rennes CONDATEAU and GeOHeLiS for their support with dissolved gases and groundwater chemistry analysis. Data for this paper is available in the Hplus database by following the permanent link: `https://doi.org/10.26169/hplus.ploemeur_field_data_dissolved_oxygen_and_iron_landscapes`.

References

Acker, J. G., & Bricker, O. P. (1992). The influence of pH on biotite dissolution and alteration kinetics at low temperature. *Geochimica et Cosmochimica Acta*, *56*(8), 3073–3092. doi: 10.1016/0016-7037(92)90290-Y

Ackerer, J., Jeannot, B., Delay, F., Weill, S., Lucas, Y., Fritz, B., … Chabaux, F. (2020). Crossing hydrological and geochemical modeling to understand the spatiotemporal variability of water chemistry in a headwater catchment (Strengbach, France). *Hydrology and Earth System Sciences*, *24*(6), 3111–3133. doi: 10.5194/hess-24-3111-2020

Antoniellini, M., Mollema, P., & Del Sole, L. (2017). Application of analytical diffusion models to outcrop observations: Implications for mass transport by fluid flow through fractures. *Water Resources Research*, *53*, 5545–5566. doi: 10.1111/j.1752-1688.1969.tb04897.x

Aquilina, L., Roques, C., Boisson, A., Vergnaud-Ayraud, V., Labasque, T., Pauwels, H., ... Bour, O. (2018). Autotrophic denitrification supported by biotite dissolution in crystalline aquifers (1): New insights from short-term batch experiments. *Science of the Total Environment*, *619-620*, 842–853. Retrieved from https://doi.org/10.1016/j.scitotenv.2017.11.079 doi: 10.1016/j.scitotenv.2017.11.079

Bar-on, Y. M., Phillips, R., & Milo, R. (2018). The biomass distribution on Earth. *Proceedings of the National Academy of Sciences of the United States of America*, *115*(25), 6506–6511. doi: 10.1073/pnas.1711842115

Bazilevskaya, E., Lebedeva, M., Pavich, M., Rother, G., Parkinson, D. Y., Cole, D., & Brantley, S. L. (2013). Where fast weathering creates thin regolith and slow weathering creates thick regolith. *Earth Surface Processes and Landforms*, *38*, 847–858. doi: 10.1002/esp.3369

Beaufort, D., Baronnet, A., Lanson, B., & Meunier, A. (1997, February). Corrensite; A single phase or a mixed-layer phyllosilicate in saponite-to-chlorite conversion series? A case study of Sancerre-Couy deep drill hole (France). *American Mineralogist*, *82*(1-2), 109–124. doi: 10.2138/am-1997-1-213

Béchennec, F., Hallégouët, B., Thiéblemont, D., & Thinon, I. (2012). *Notice explicative, Carte géol France (1/50 000), feuille Lorient (383)* (BRGM, Ed.). Orléans: BRGM.

Behrens, R., Bouchez, J., Schuessler, J. A., Dultz, S., Hewawasam, T., & Von Blanckenburg, F. (2015). Mineralogical transformations set slow weathering rates in low-porosity metamorphic bedrock on mountain slopes in a tropical climate. *Chemical Geology*, *411*, 283–298. Retrieved from http://dx.doi.org/10.1016/j.chemgeo.2015.07.008 doi: 10.1016/j.chemgeo.2015.07.008

Belghoul, A. (2010). *Caractérisation pétrophysique et hydrodynamique du socle cristalli* (Unpublished doctoral dissertation).

Bethencourt, L., Bochet, O., Farasin, J., Aquilina, L., Borgne, T. L., Quaiser, A., ... Dufresne, A. (2020). Genome reconstruction reveals distinct assemblages of Gallionellaceae in surface and subsurface redox transition zones. *FEMS Microbiology Ecology*, *96*(5). doi: 10.1093/femsec/fiaa036

Bochet, O., Bethencourt, L., Dufresne, A., Farasin, J., Pédrot, M., Labasque, T., ... Le Borgne, T. (2020, feb). Iron-oxidizer hotspots formed by intermittent oxic–anoxic fluid mixing in fractured rocks. *Nature Geoscience*, *13*(2), 149–155. doi: 10.1038/s41561-019-0509-1

Bucher, K., Zhu, Y., & Stober, I. (2009, October). Groundwater in fractured crystalline rocks, the Clara mine, Black Forest (Germany). *International Journal of Earth Sciences*, *98*(7), 1727–1739. doi: 10.1007/s00531-008-0328-x

Casar, C. P., Momper, L. M., Kruger, B. R., & Osburn, M. R. (2021). Iron-Fueled Life in the Continental Subsurface : Deep Mine. *Applied and Environmental Microbiology*, *87*(20).

Dalsgaard, T., Stewart, F. J., Thamdrup, B., De Brabandere, L., Revsbech, N. P., Ulloa, O., ... DeLong, E. F. (2014, October). Oxygen at Nanomolar Levels Reversibly Suppresses Process Rates and Gene Expression in Anammox and Denitrification in the Oxygen Minimum Zone off Northern Chile. *mBio*, *5*(6), e01966-14. doi: 10.1128/mBio.01966-14

Deng, H., & Spycher, N. (2019). Modeling reactive transport processes in fractures.

Reviews in Mineralogy and Geochemistry, *85*(1), 49–74. doi: 10.2138/rmg.2019.85.3

DeSimone, L., Mcmahon, P. B., & Rosen, M. (2014). *The quality of our Nation's waters - Water quality in Principal Aquifers of the United States, 1991-2010* (Tech. Rep.). U.S. Geological Survey Circular 1360. doi: https://doi.org/10.3133/cir1360

Dideriksen, K., Christiansen, B. C., Frandsen, C., Balic-Zunic, T., Mørup, S., & Stipp, S. L. S. (2010, May). Paleo-redox boundaries in fractured granite. *Geochimica et Cosmochimica Acta*, *74*(10), 2866–2880. doi: 10.1016/j.gca.2010.02.022

Druschel, G. K., Emerson, D., Sutka, R., Suchecki, P., & Luther, G. W. (2008). Low-oxygen and chemical kinetic constraints on the geochemical niche of neutrophilic iron(II) oxidizing microorganisms. *Geochimica et Cosmochimica Acta*, *72*(14), 3358–3370. doi: 10.1016/j.gca.2008.04.035

Edmunds, W. M., Miles, D., & Cook, J. (1984). A comparative study of sequential redox processes in three British aquifers. *Hydrochemical balances of freshwater systems*, *50*, 55–70.

Emerson, D., Fleming, E. J., & McBeth, J. M. (2010). Iron-Oxidizing Bacteria: An Environmental and Genomic Perspective. *Annual Review of Microbiology*, *64*(1), 561–583. doi: 10.1146/annurev.micro.112408.134208

Erable, B., Féron, D., & Bergel, A. (2012). Microbial catalysis of the oxygen reduction reaction for microbial fuel cells: A review. *ChemSusChem*, *5*(6), 975–987. doi: 10.1002/cssc.201100836

Fletcher, R. C., Buss, H. L., & Brantley, S. L. (2006). A spheroidal weathering model coupling porewater chemistry to soil thicknesses during steady-state denudation. *Earth and Planetary Science Letters*, *244*(1-2), 444–457. doi: 10.1016/j.epsl.2006.01.055

Frey, P. A., & Reed, G. H. (2012). The ubiquity of iron. *ACS Chemical Biology*, *7*(9), 1477–1481. doi: 10.1021/cb300323q

Goldich, S. S. (1938, January). A Study in Rock-Weathering. *The Journal of Geology*, *46*(1), 17–58. doi: 10.1086/624619

Gu, X., Heaney, P. J., Reis, F. D., & Brantley, S. L. (2020). Deep abiotic weathering of pyrite. *Science (New York, N.Y.)*, *370*(6515). doi: 10.1126/science.abb8092

Guillaumot, L., Longuevergne, L., Marçais, J., Lavenant, N., & Bour, O. (2022, June). Frequency domain water table fluctuations reveal recharge in fractured aquifers depends on both intense and seasonal rainfall and unsaturated zone thickness. *Hydrology and Earth System Sciences Discussions*, 1–38. doi: 10.5194/hess-2022-201

Hampl, F. J., Schiperski, F., Byrne, J. M., Schwerdhelm, C., Kappler, A., Bryce, C., ... Neumann, T. (2021). The role of iron-bearing minerals for the deep weathering of a hydrothermally altered plutonic rock in semi-arid climate (chilean coastal cordillera). *Chemical Geology*. Retrieved from `https://doi.org/10.1016/j.scitotenv.2020.141163` doi: 10.1016/j.chemgeo.2022.120922

Hancock, P. J., Boulton, A. J., & Humphreys, W. F. (2005). Aquifers and hyporheic zones: Towards an ecological understanding of groundwater. *Hydrogeology Journal*, *13*(1), 98–111. doi: 10.1007/s10040-004-0421-6

Hartmann, J., & Moosdorf, N. (2012). The new global lithological map database GLiM: A representation of rock properties at the Earth surface. *Geochemistry, Geophysics, Geosystems*, *13*(12), 1–37. doi: 10.1029/2012GC004370

Helgeson, H. C., Garrels, R. M., & MacKenzie, F. T. (1969, April). Evaluation of irreversible reactions in geochemical processes involving minerals and aqueous solutions—II. Applications. *Geochimica et Cosmochimica Acta*, *33*(4), 455–481. doi: 10.1016/0016-7037(69)90127-6

Holbrook, W. S., Marcon, V., Bacon, A. R., Brantley, S. L., Carr, B. J., Flinch,

B. A., . . . Riebe, C. S. (2019). Links between physical and chemical weathering inferred from a 65-m-deep borehole through Earth's critical zone. *Scientific Reports*, *9*, 1–11. doi: 10.1038/s41598-019-40819-9

Humphreys, W. F. (2009). Hydrogeology and groundwater ecology: Does each inform the other? *Hydrogeology Journal*, *17*(1), 5–21. doi: 10.1007/s10040-008-0349-3

Jiménez-Martínez, J., Longuevergne, L., Le Borgne, T., Davy, P., Russian, A., & Bour, O. (2013, may). Temporal and spatial scaling of hydraulic response to recharge in fractured aquifers: Insights from a frequency domain analysis. *Water Resources Research*, *49*(5), 3007–3023. Retrieved from `http://doi.wiley.com/10.1002/wrcr.20260` doi: 10.1002/wrcr.20260

Kappler, A., Bryce, C., Mansor, M., Lueder, U., Byrne, J. M., & Swanner, E. D. (2021). An evolving view on biogeochemical cycling of iron. *Nature Reviews Microbiology*, *19*(6), 360–374. Retrieved from `http://dx.doi.org/10.1038/s41579-020-00502-7` doi: 10.1038/s41579-020-00502-7

Kartsen Pedersen. (1997). Microbial life in deep granitic rock. *FEMS microbiology reviews*, *20*(3-4), 399–414. doi: 10.1016/S0168-6445(97)00022-3

Kim, H., Stinchcomb, G., & Brantley, S. L. (2017). Feedbacks among O2 and CO2 in deep soil gas , oxidation of ferrous minerals , and fractures : A hypothesis for steady-state regolith thickness. *Earth and Planetary Science Letters*, *460*, 29–40. Retrieved from `http://dx.doi.org/10.1016/j.epsl.2016.12.003` doi: 10.1016/j.epsl.2016.12.003

Kolbe, T., De Dreuzy, J. R., Abbott, B. W., Aquilina, L., Babey, T., Green, C. T., . . . Pinay, G. (2019). Stratification of reactivity determines nitrate removal in groundwater. *Proceedings of the National Academy of Sciences of the United States of America*, *116*(7), 2494–2499. doi: 10.1073/pnas.1816892116

Korom, S. F. (1992). Natural denitrification in the saturated zone: A review. *Water Resources Research*, *28*(6), 1657–1668. doi: 10.1029/92WR00252

Krone, L. V., Hampl, F. J., Schwerdhelm, C., Bryce, C., Ganzert, L., Kitte, A., . . . von Blanckenburg, F. (2021). Deep weathering in the semi-arid Coastal Cordillera, Chile. *Scientific Reports*, *11*(1), 1–15. Retrieved from `https://doi.org/10.1038/s41598-021-90267-7` doi: 10.1038/s41598-021-90267-7

Lasaga, A. C. (1984). Chemical kinetics of water-rock interactions. *Journal of Geophysical Research: Solid Earth*, *89*(B6), 4009–4025. Retrieved from `http://doi.wiley.com/10.1029/JB089iB06p04009` doi: 10.1029/JB089iB06p04009

Le Borgne, T., Bour, O., Riley, M. S., Gouze, P., Pezard, P. A., Belghoul, A., . . . Last, B. J. (2007). Comparison of alternative methodologies for identifying and characterizing preferential flow paths in heterogeneous aquifers. *Journal of Hydrology*, *345*(3-4), 134–148. doi: 10.1016/j.jhydrol.2007.07.007

Leray, S., de Dreuzy, J.-R., Aquilina, L., Vergnaud-Ayraud, V., Labasque, T., Bour, O., & Le Borgne, T. (2014). Temporal evolution of age data under transient pumping conditions. *Journal of Hydrology*, *511*, 555–566.

Leray, S., de Dreuzy, J. R., Bour, O., & Bresciani, E. (2013). Numerical modeling of the productivity of vertical to shallowly dipping fractured zones in crystalline rocks. *Journal of Hydrology*, *481*, 64–75. Retrieved from `http://dx.doi.org/10.1016/j.jhydrol.2012.12.014` doi: 10.1016/j.jhydrol.2012.12.014

Li, L., Maher, K., Navarre-sitchler, A., Druhan, J., Meile, C., Lawrence, C., . . . Beisman, J. (2017). Expanding the role of reactive transport models in critical zone processes. *Earth-Science Reviews*, *165*, 280–301. doi: 10.1016/j.earscirev.2016.09.001

Macquarrie, K. T. B., Mayer, K. U., Jin, B., & Spiessl, S. M. (2010). The importance of conceptual models in the reactive transport simulation of oxygen ingress in sparsely fractured crystalline rock. *Journal of Contaminant Hydrology*, *112*(1-4), 64–76. Retrieved from `http://dx.doi.org/10.1016/j.jconhyd.2009.10.007` doi: 10.1016/j.jconhyd.2009.10.007

Mader, M., Schmidt, C., van Geldern, R., & Barth, J. A. (2017). Dissolved oxygen in water and its stable isotope effects: A review. *Chemical Geology*, *473*(September), 10–21. Retrieved from `http://dx.doi.org/10.1016/j.chemgeo.2017.10.003` doi: 10.1016/j.chemgeo.2017.10.003

Maher, K. (2010). The dependence of chemical weathering rates on fluid residence time. *Earth and Planetary Science Letters*, *294*(1-2), 101–110. Retrieved from `http://dx.doi.org/10.1016/j.epsl.2010.03.010` doi: 10.1016/j.epsl.2010.03.010

Maher, K., & Chamberlain, C. P. (2014, March). Hydrologic Regulation of Chemical Weathering and the Geologic Carbon Cycle. *Science*, *343*(6178), 1502–1504. doi: 10.1126/science.1250770

Maisch, M., Lueder, U., Laufer, K., Scholze, C., Kappler, A., & Schmidt, C. (2019). Contribution of Microaerophilic Iron(II)-Oxidizers to Iron(III) Mineral Formation. *Environmental Science and Technology*, *53*(14), 8197–8204. doi: 10.1021/acs.est.9b01531

Malard, F., & Hervant, F. (1999). Oxygen supply and the adaptations of animals in groundwater. *Freshwater Biology*, *41*, 1 – 30.

Malmstrom, M., Banwart, S., Duro, L., Wersin, P., & Bruno, J. (1995). *Biotite and Chlorite Weathering at 25ºC* (Tech. Rep. No. January).

Malmström, M., Banwart, S., Lewenhagen, J., Duro, L., & Bruno, J. (1996). The dissolution of biotite and chlorite at 25 ºC in the near-neutral pH region. *Journal of Contaminant Hydrology*, *21*, 201–213.

Melton, E. D., Swanner, E. D., Behrens, S., Schmidt, C., & Kappler, A. (2014). The interplay of microbially mediated and abiotic reactions in the biogeochemical Fe cycle. *Nature Reviews Microbiology*, *12*(12), 797–808. Retrieved from `http://dx.doi.org/10.1038/nrmicro3347` doi: 10.1038/nrmicro3347

Molenat, J., Davy, P., Gascuel-Odoux, C., & Durand, P. (1999). Study of Three Subsurface Hydrologic Systems Based on Spectral and Cross-Spectral Analysis of Time Series. *Journal of Hydrology*, *222*, 152–164.

Murakami, T., Utsunomiya, S., Yokoyama, T., & Kasama, T. (2003). Biotite dissolution processes and mechanisms in the laboratory and in nature: Early stage weathering environment and vermiculitization. *American Mineralogist*, *88*(2-3), 377–386. doi: 10.2138/am-2003-2-314

Napieralski, S. A., Buss, H. L., Brantley, S. L., Lee, S., Xu, H., & Roden, E. E. (2019). Microbial chemolithotrophy mediates oxidative weathering of granitic bedrock. *Proceedings of the National Academy of Sciences of the United States of America*, *116*(52), 26394–26401. doi: 10.1073/pnas.1909970117

Nordstrom, D. K. (2011). Hydrogeochemical processes governing the origin, transport and fate of major and trace elements from mine wastes and mineralized rock to surface waters. *Applied Geochemistry*, *26*(11), 1777–1791. Retrieved from `http://dx.doi.org/10.1016/j.apgeochem.2011.06.002` doi: 10.1016/j.apgeochem.2011.06.002

Palandri, J., & Kharaka, Y. (2004). *A Compilation of Rate Parameters of Water-Mineral Interaction Kinetics* (Vol. REPORT 200; Tech. Rep.).

Petsch, S. T., Bolton, E., Mok, U., & Evans, B. (2004). The weathering of sedimentary organic matter as a control on athmospheric O2 : I . Analysis of a black shale. *American Journal of Science*, *304*, 234–249.

Robie A., R., & Philip M., B. (1962). *Molar Volumes and Densities of Minerals - TEI-822* (Tech. Rep.). USGS.

Roques, C., Aquilina, L., Boisson, A., Vergnaud-Ayraud, V., Labasque, T., Longuevergne, L., . . . Bour, O. (2018). Autotrophic denitrification supported by biotite dissolution in crystalline aquifers: (2) transient mixing and denitrification dynamic during long-term pumping. *Science of the Total Environment*, *619-620*, 491–503. Retrieved from `https://doi.org/10.1016/j.scitotenv.2017.11.104` doi: 10.1016/j.scitotenv.2017.11.104

Roques, C., Bour, O., Aquilina, L., & Dewandel, B. (2016). High-yielding aquifers in crystalline basement: insights about the role of fault zones, exemplified by Armorican Massif, France. *Hydrogeology Journal*, *24*(8), 2157–2170. doi: 10.1007/s10040-016-1451-6

Ruelleu, S., Moreau, F., Bour, O., Gapais, D., & Martelet, G. (2010). Impact of gently dipping discontinuities on basement aquifer recharge: An example from Ploemeur (Brittany, France). *Journal of Applied Geophysics*, *70*(2), 161–168. Retrieved from `http://dx.doi.org/10.1016/j.jappgeo.2009.12.007` doi: 10.1016/j.jappgeo.2009.12.007

Ruff, S. E., Humez, P., Angelis, I. H. D., Nightingale, M., Diao, M., Connors, L., ... Strous, M. (2022). Hydrogen and dark oxygen drive microbial productivity in diverse groundwater ecosystems. *bioRxiv*. doi: 10.1101/2022.08.09.503387

Scott, A. D., & Amonette, J. (1985). Role of Iron in Mica Weathering. In *Iron in soils and clay minerals* (pp. 537–605). Bad Windsheim: Reidel Publishing Company. doi: 10.1007/978-94-009-4007-9

Seeboonruang, U., & Ginn, T. R. (2006). Upscaling heterogeneity in aquifer reactivity via exposure-time concept: Forward model. *Journal of contaminant hydrology*, *84*(3-4), 127–154.

Sequeira Braga, M. A., Paquet, H., & Begonha, A. (2002, August). Weathering of granites in a temperate climate (NW Portugal): Granitic saprolites and arenization. *CATENA*, *49*(1), 41–56. doi: 10.1016/S0341-8162(02)00017-6

Serikov, L. V., Tropina, E. A., Shiyan, L. N., Frimmel, F. H., Metreveli, G., & Delay, M. (2009). Iron oxidation in different types of groundwater of Western Siberia. *Journal of Soils and Sediments*, *9*(2), 103–110. doi: 10.1007/s11368-009-0069-x

Sidborn, M., & Neretnieks, I. (2007). Long term redox evolution in granitic rocks: Modelling the redox front propagation in the rock matrix. *Applied Geochemistry*, *22*(11), 2381–2396. doi: 10.1016/j.apgeochem.2007.05.007

Sidborn, M., & Neretnieks, I. (2008). Long-term oxygen depletion from infiltrating groundwaters: Model development and application to intra-glaciation and glaciation conditions. *Journal of Contaminant Hydrology*, *100*(1-2), 72–89. doi: 10.1016/j.jconhyd.2008.05.010

Singer, P. C., & Stumm, W. (1970). Acidic Mine Drainage: The Rate-Determining Step. *Science*, *167*(3921), 1121–1123.

Singha, K., & Navarre-Sitchler, A. (2022). The Importance of Groundwater in Critical Zone Science. *Groundwater*, *60*(1), 27–34. doi: 10.1111/gwat.13143

Steefel, C. I., & Maher, K. (2009). Fluid-rock interaction: A reactive transport approach. *Reviews in Mineralogy and Geochemistry*, *70*(1), 485–532. Retrieved from `https://cloudfront.escholarship.org/dist/prd/content/qt61m6h3gd/qt61m6h3gd.pdf?t=li62lc`

Stumm, W., & Morgan, J. J. (1996). Oxidation and Reduction: Equilibria and Microbial Mediation. In J. Schnoor & A. Zehnder (Eds.), *Aquatic chemistry: Chemical equilibria and rates in natural waters* (3rd ed., pp. 425–515). Wiley.

Sugimori, H., Iwatsuki, T., & Murakami, T. (2008). Chlorite and biotite weathering, Fe2+-rich corrensite formation, and Fe behavior under low Po2 conditions and thier implication for precambrian weathering. *American Mineralogist*, *93*(7), 1080–1089. doi: 10.2138/am.2008.2663

Sullivan, P. L., Hynek, S. A., Gu, X., Singha, K., White, T., West, N., ... Brantley, S. L. (2016). Oxidative dissolution under the channel leads geomorphological evolution at the shale hills catchment. *American Journal of Science*, *316*(10), 981–1026. doi: 10.2475/10.2016.02

Tebo, B. M., Johnson, H. A., McCarthy, J. K., & Templeton, A. S. (2005). Geomicrobiology of manganese(II) oxidation. *Trends in Microbiology*, *13*(9), 421–428. doi: 10.1016/j.tim.2005.07.009

Touchard, F. (1999). *Caractérisation hydrogéologique d'un aquifère de socle fracturé*

: Site de Ploemeur (Morbihan). (Doctoral dissertation, Université de Rennes 1). Retrieved from https://tel.archives-ouvertes.fr/tel-00675884/file/Touchard.pdf

Trinchero, P., Molinero, J., Ebrahimi, H., Puigdomenech, I., Gylling, B., Svensson, U., ... Deissmann, G. (2018). Simulating Oxygen Intrusion into Highly Performance Computing. *Mathematical Geosciences*, 49–51. Retrieved from https://doi.org/10.1007/s11004-017-9718-6 doi: 10.1007/s11004-017-9718-6

Trinchero, P., Sidborn, M., & Puigdomenech, I. (2018). Comment on "Application of Analytical Diffusion Models to Outcrop Observations: Implications for Mass Transport by Fluid Flow Through Fractures" by Antonellini et al. (2017). *Water Resources Research*, *54*(11), 9702–9705. doi: 10.1029/2018WR023122

Trinchero, P., Sidborn, M., Puigdomenech, I., Svensson, U., Ebrahimi, H., Molinero, J., ... Deissmann, G. (2019). Transport of oxygen into granitic rocks: Role of physical and mineralogical heterogeneity. *Journal of Contaminant Hydrology*, *220*(November 2018), 108–118. Retrieved from https://doi.org/10.1016/j.jconhyd.2018.12.001 doi: 10.1016/j.jconhyd.2018.12.001

White, A. F., & Yee, A. (1985). Aqueous oxidation-reduction kinetics associated with coupled electron-cation transfer from iron-containing silicates at 25°C. *Geochimica et Cosmochimica Acta*, *49*(5), 1263–1275. doi: 10.1016/0016-7037(85)90015-8

White, A. F., Yee, A., & Flexser, S. (1985). Surface oxidation-reduction kinetics associated with experimental basalt-water reaction at 25°C. *Chemical Geology*, *49*(1-3), 73–86. doi: 10.1016/0009-2541(85)90148-2

Wild, B., Daval, D., Beaulieu, E., Pierret, M. C., Viville, D., & Imfeld, G. (2019). In-situ dissolution rates of silicate minerals and associated bacterial communities in the critical zone (Strengbach catchment, France). *Geochimica et Cosmochimica Acta*, *249*, 95–120. doi: 10.1016/j.gca.2019.01.003

Winograd, I., & Robertson, F. (1982). Deep Oxygenated Ground Water : Anomaly or Common Occurrence? *Science*, *216*(4551), 1227–1230. doi: 10.1126/science.216.4551.1227

Wolthoorn, A., Temminghoff, E. J., Weng, L., & Van Riemsdijk, W. H. (2004). Colloid formation in groundwater: Effect of phosphate, manganese, silicate and dissolved organic matter on the dynamic heterogeneous oxidation of ferrous iron. *Applied Geochemistry*, *19*(4), 611–622. doi: 10.1016/j.apgeochem.2003.08.003

Supplementary material

Ivan Osorio-Leon[1]**, Camille Bouchez**[1]**, Eliot Chatton**[1]**, Nicolas Lavenant**[1]**, Laurent Longuevergne**[1]**, Tanguy Le Borgne**[1]

[1]Univ Rennes – CNRS, Géosciences Rennes - UMR 6118. Rennes, France

1 Data availability

Data for this paper is available in the Hplus database by following the permanent link `https://hplus.ore.fr/en/osorio-leon-et-al-2022-wrr-data`

2 Input compositions of water and rock for the base case simulation with the numerical model

Table 1. Input water composition for the numerical model

Temperature [ºC]	16	
pH	7	
	Concentrations	[mol/kg]
$O_2(aq)$		2.6×10^{-2}
Cl^-		1.9×10^{-3}
SO_4^{2-}		3.0×10^{-4}
Na^+		2.2×10^{-3}
Mg^{2+}		5.3×10^{-4}
Al^{3+}		8.9×10^{-8}
H_4SiO_4		2.2×10^{-4}
K^+		9.2×10^{-5}
Ca^{2+}		2.5×10^{-4}
Fe^{2+}		0.0
$CO_2(aq)$		4.3×10^{-5}

3 Mineral stability diagram

4 Dissolved iron measurements

Major and trace cations were quantified by Inductively Coupled Plasma Mass Spectroscopy (Agilent Technologies, 7700x) in pre-acidified and 0.2 μm-filtered samples. Uncertainties were between 2 to 5%. Major anion samples (non-acidified) were analyzed by Ionic Chromatography (Dionex DX-120) with uncertainties below 4%. Groundwater sampling consisted on descending a submersible MP1 pump (Grundfos) until the depth of the dominant fracture in the borehole. Physicochemical parameters in the pump discharge were monitored with a WTW probe. Groundwater was sampled after the monitored parameters were stable.

Corresponding author: Ivan-David Osorio-Leon, `ivan-david.osorio-leon@univ-rennes1.fr`

Corresponding author: Camille Bouchez, `camille.bouchez@univ-rennes1.fr`

Table 2. Mineralogical composition used as input for the numerical simulations. *Diss Only* indicates that only dissolution is allowed and *tst* indicates that both dissolution and precipitation can occur. Kinetic and thermodynamic parameters for Equation (4) are taken from the database files of the Thermoddem project (Blanc et al., 2012) and from Palandri and Kharaka (2004).

Mineral	Structural formula	Mineral volume fraction $[\Phi_j]$	Reaction type
Primary minerals			
Albite	$NaAlSi_3O_8$	0.000	TST - Diss only
Quartz	SiO_2	0.444	TST - Diss only
K-Feldspar	$KAlSi_3O_8$	0.297	TST - Diss only
Biotite	$K(Mg_2Fe^{II})(Si_3Al)O_{10}(OH)_2$	0.099	TST - Diss only
Muscovite	$KAl_2(AlSi_3O_{10})(OH)_2$	0.149	TST - Diss only
Secondary minerals			
Chlorite	$(Mg_3Fe_2^{II}Al)(Si_3Al)O_{10}(OH)_8$	1×10^{-5}	TST
Kaolinite	$Al_2Si_2O_5(OH)_4$	0.000	TST
Goethite	$Fe^{III}OOH$	0.000	TST

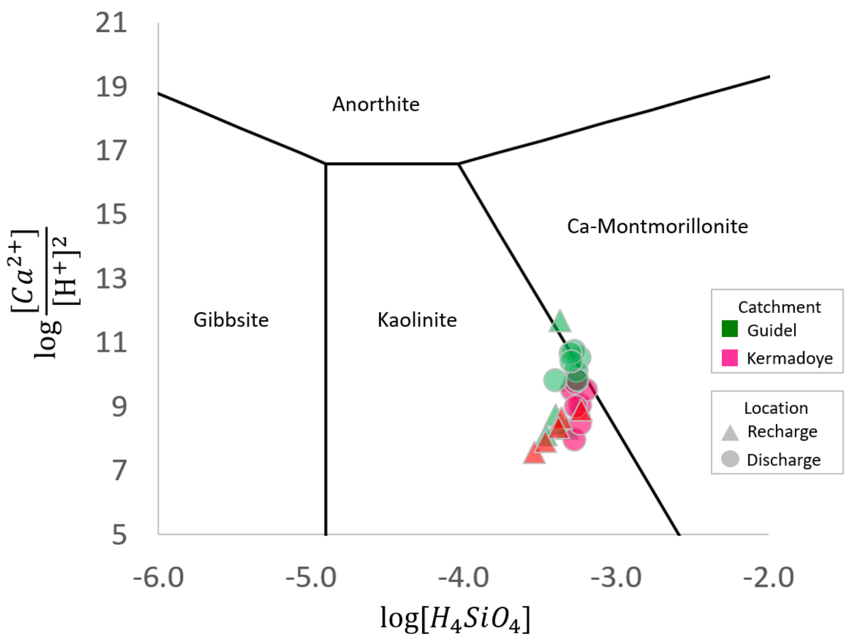

Figure 1. Mineral stability diagram

5 Depth of the groundwater reservoir

Since fracture networks are highly heterogeneous features (Le Borgne et al., 2006), one cannot directly rely the depth of an intersected fracture in a borehole with the representative depth of the circulating fluid's reservoir. For instance, at the site scale, normal faults dipping of about 70º (Ruelleu et al., 2010) will globally favor subvertical circulations. At a more restricted scale, a fracture analysis in a borehole from the Guidel catchment (Bochet et al., 2020) has shown that fracture's dip can vary from 20 to 80º.

Following this, we have used the groundwater's temperature as a proxy of depth. Hence, the depth of the reservoir of the groundwater circulating in a fracture ($Depth_{proxy}$) was calculated as:

$$Depth_{proxy} = \frac{T - T_{rech}}{G_G}$$

T corresponds to groundwater temperature as measured from borehole logs, T_{rech} corresponds to the average recharge temperature of the Ploemeur site, that is 12 ºC, as deduced from the average temperature in the weather station, and G_G corresponds to the Geothermal Gradient. For the Ploemeur site, G_G has been considered as 0.013 $^\circ C.m^{-1}$ after (Pouladi et al., 2021).

6 Sensitivity of $Depth_{proxy}$ estimates

We note that the depth estimates for the DO measurements presented in Figure 7 rely on using groundwater's temperature as a proxy for depth ($Depth_{proxy}$). As estimated, $Depth_{proxy}$ depends on two site-dependent parameters, i.e. the average recharge temperature (T_{rech}) and the Geothermal Gradient (G_G). Both parameters are mostly invariant at short timescales and are not easily measurable. As a result, uncertainties around their value come from measurements rather than seasonality or natural disturbances. The CZO of Ploemeur is a well-studied site and both T_{rech} and G_G are well constrained, allowing to reduce incertitude's around their value. The average value for T_{rech} has been estimated to be 12.2±0.41 $^\circ C$ as deduced from temperature time-series (from 2002 to 2018) recorded at the weather station in the Ploemeur CZO. On the other hand, previous works suggest that the G_G of the Ploemeur site ranges between 0.016 and 0.013 $^\circ C.m^{-1}$ (Pouladi et al., 2021; Klepikova et al., 2011) and for this work we considered the most recent estimate of 0.013 $^\circ C.m^{-1}$ after Pouladi et al. (2021).

It is important to notice that the estimated $Depth_{proxy}$ is highly sensitive to both parameters and it can thus directly impact the estimated depth of the oxygenated zone in the aquifer. For instance, if one considers the borehole with the highest temperature (and thus the deepest $Depth_{proxy}$) from Figure 7 (from main text), and by combining the uncertainties of T_{rech} and G_G , the maximum depth in which oxygen has been detected in this study can oscillate between 333 m and 473 m below surface.

6.1 Effect of velocity on oxic iron concentrations

Figure 2 shows how, for a same Damköhler number, the variations in the apparent vertical velocity impacts the iron concentrations at oxic conditions according to Equation 19 in main text. Predicted concentrations are restricted to low values because they are limited by the fast oxidation of iron by oxygen. Note that they are close to the detection limit of ICPMS analysis that usually is close to 10^{-4} ppb. This makes difficult to constrain the apparent vertical velocity by using the iron concentration data, yet it is possible if analytical methods for iron are sensible enough.

7 Borehole logs

7.1 Methods

Multiparameter borehole logs under ambient conditions (dissolved oxygen, temperature, electrical conductivity and pH) acquired since 2003, available in the database of the French network of hydrogeological research sites (`https://hplus.ore.fr/en/`), were used as base for exploring the physicochemical parameters with depth. This dataset was completed with two additional field campaigns in order to validate the historical data. Multiparameter borehole logs in ambient conditions were acquired at two different times of the hydrologic year: high groundwater level's season (late fall 2022) and low level's season (late spring 2021) using an Idronaut Ocean Seven multiparameter probe. The instrument was calibrated following the manufacturer's specification and the accuracy of

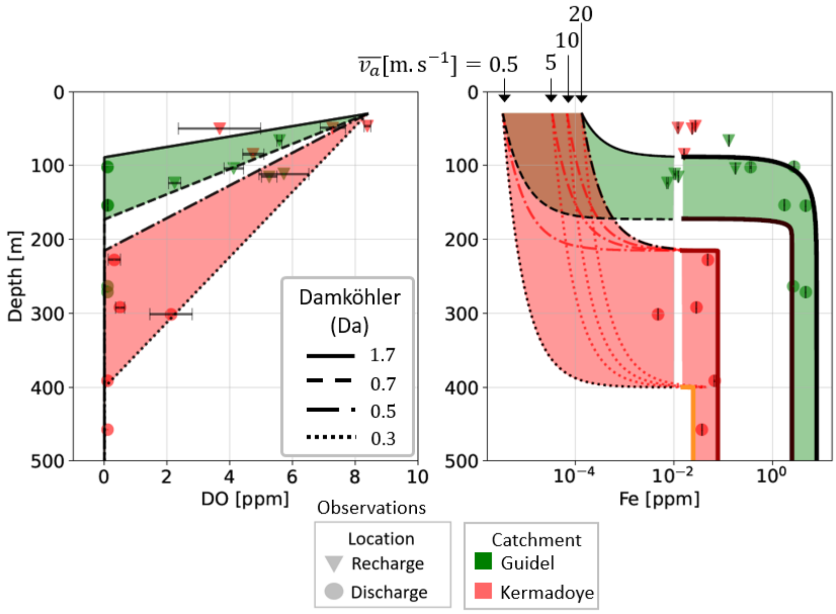

Figure 2. Effect of vertical velocity on the predicted iron concentrations at oxic concentrations

the DO probe (± 0.1 $mg.L^{-1}$) was crosschecked by gas chromatography analyses at the University of Rennes 1 (Figure 3).

7.2 logs per borehole

The following figures present the synthesis of multiparameter logs for every borehole. The shaded areas correspond to the tubewall while the white areas correspond the slotted sections. The horizontal dash-dotted lines correspond to fractures intersected in the borehole (black for the main fracture, grey for secondary fractures).

The legend in every plot indicate the mode of log-acquisition (”up” for upwards, down for ”downwards”), the date, and the name of the multiparameter probe.

f9

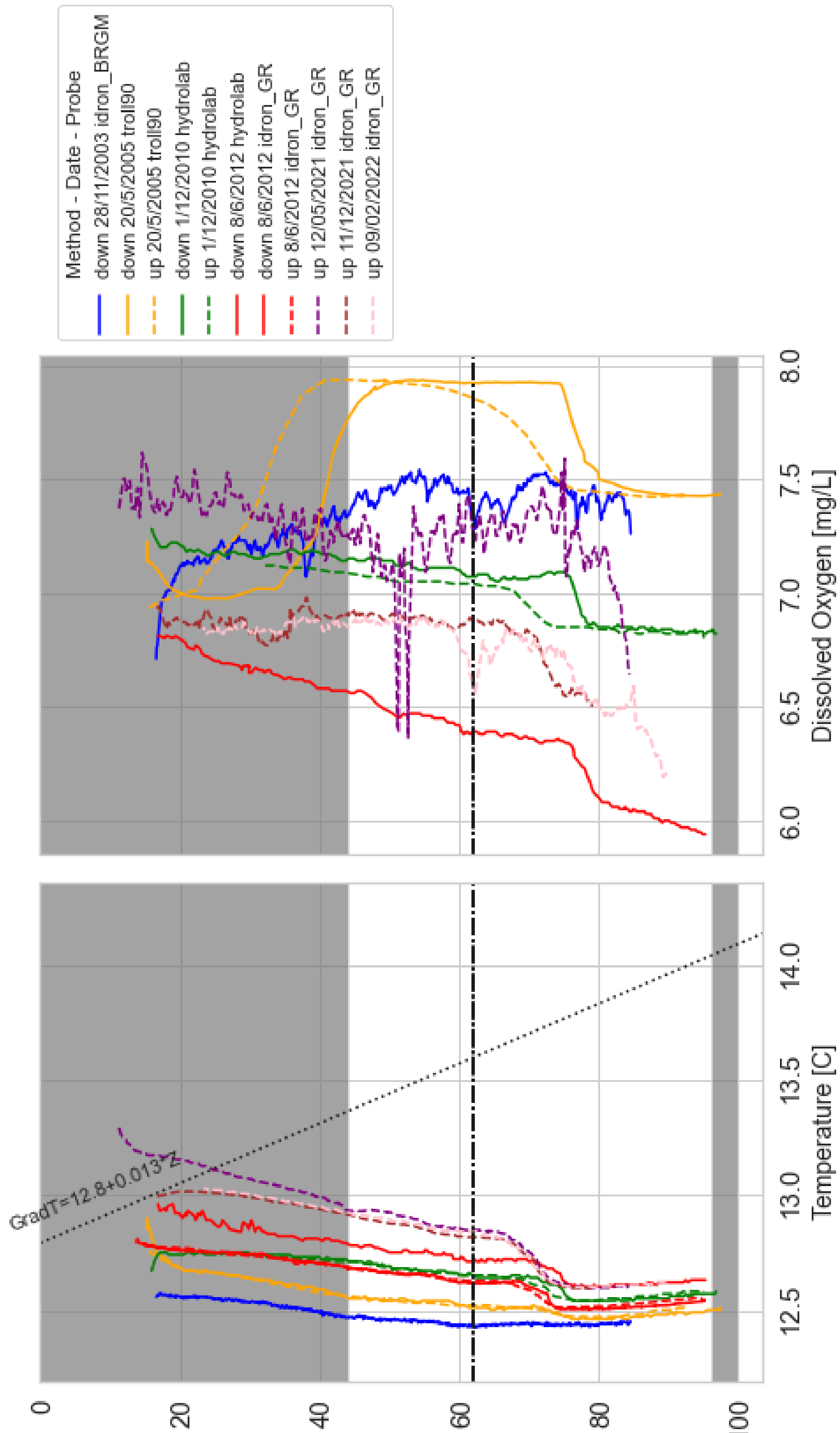
Method - Date - Probe
down 28/11/2003 idron_BRGM
down 20/5/2005 troll90
up 20/5/2005 troll90
down 1/12/2010 hydrolab
up 1/12/2010 hydrolab
down 8/6/2012 hydrolab
down 8/6/2012 idron_GR
up 8/6/2012 idron_GR
up 12/05/2021 idron_GR
up 11/12/2021 idron_GR
up 09/02/2022 idron_GR
GradT=12.8+0.013*Z
Depth to ref (m TVD)
0
20
40
60
80
100
12.5
13.0
13.5
14.0
Temperature [C]
6.0
6.5
7.0
7.5
8.0
Dissolved Oxygen [mg/L]

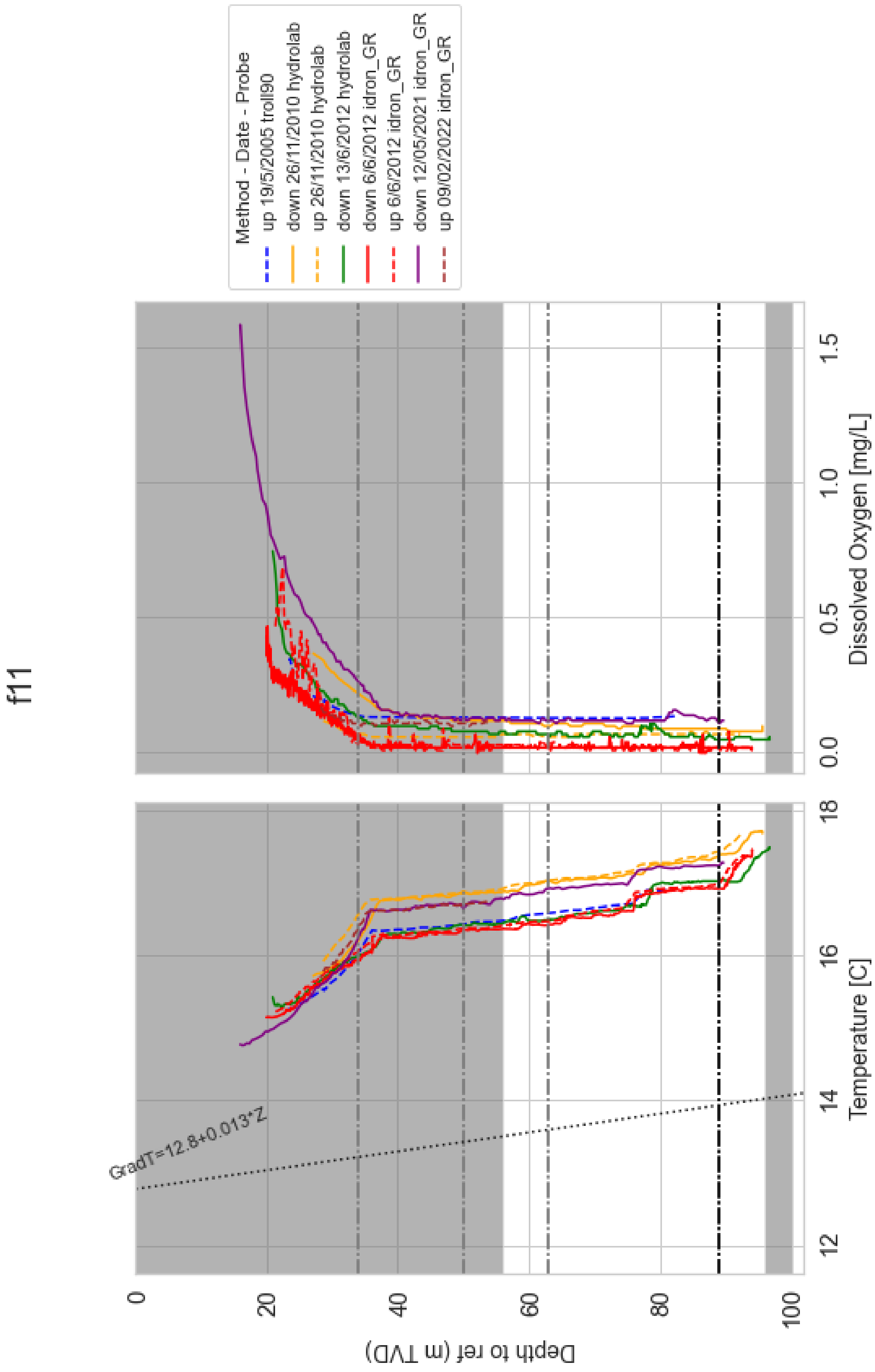
f11
Method - Date - Probe
up 19/5/2005 troll90
down 26/11/2010 hydrolab
up 26/11/2010 hydrolab
down 13/6/2012 hydrolab
down 6/6/2012 idron_GR
up 6/6/2012 idron_GR
down 12/05/2021 idron_GR
up 09/02/2022 idron_GR
GradT=12.8+0.013*Z
Depth to ref (m TVD)
0
20
40
60
80
100
12
14
16
18
Temperature [C]
0.0
0.5
1.0
1.5
Dissolved Oxygen [mg/L]

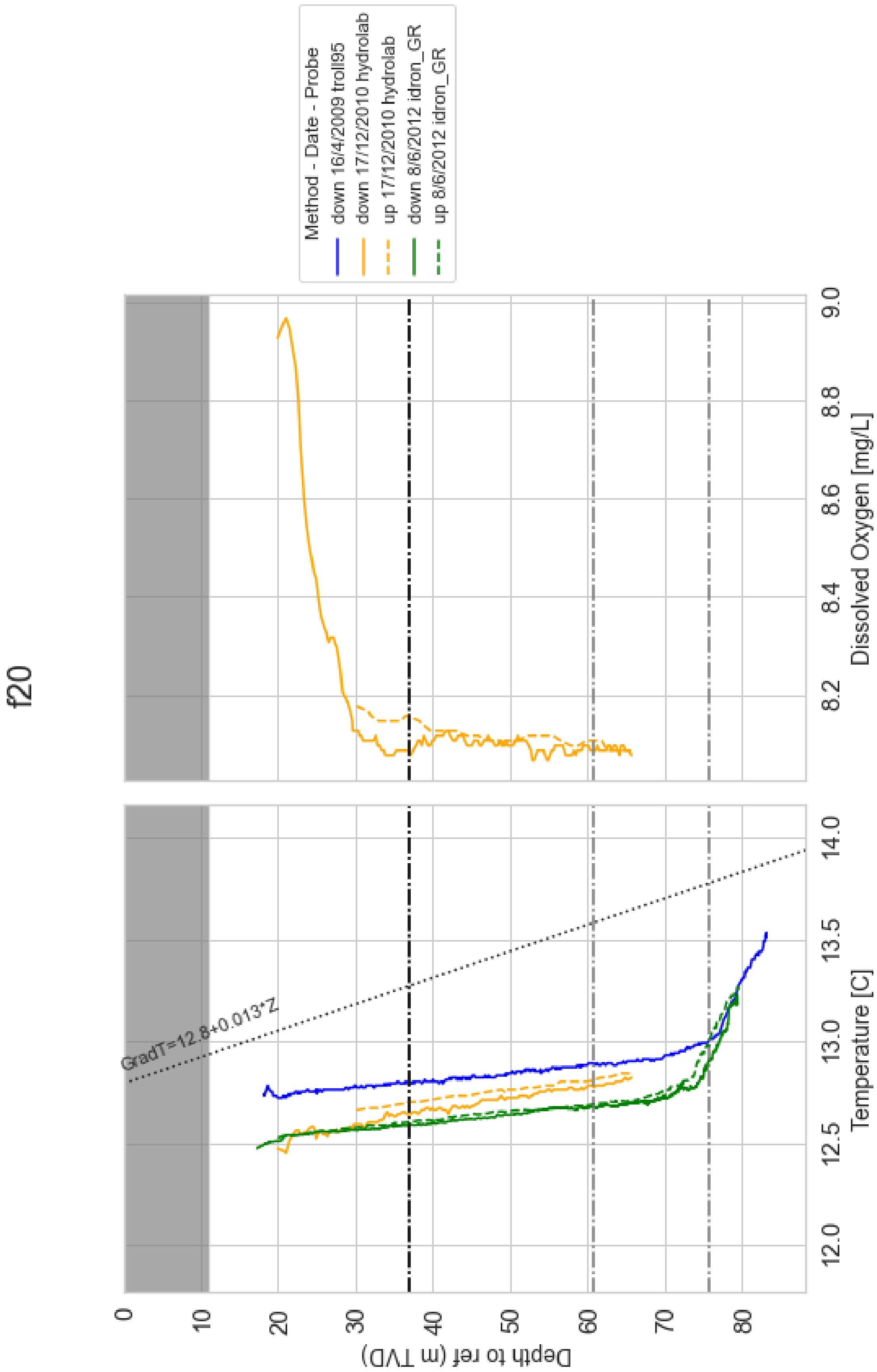
f20
Method - Date - Probe
down 16/4/2009 troll95
down 17/12/2010 hydrolab
up 17/12/2010 hydrolab
down 8/6/2012 idron_GR
up 8/6/2012 idron_GR
GradT=12.8+0.013*Z
Depth to ref (m TVD)
Temperature [C]
Dissolved Oxygen [mg/L]
0
10
20
30
40
50
60
70
80
12.0
12.5
13.0
13.5
14.0
8.2
8.4
8.6
8.8
9.0

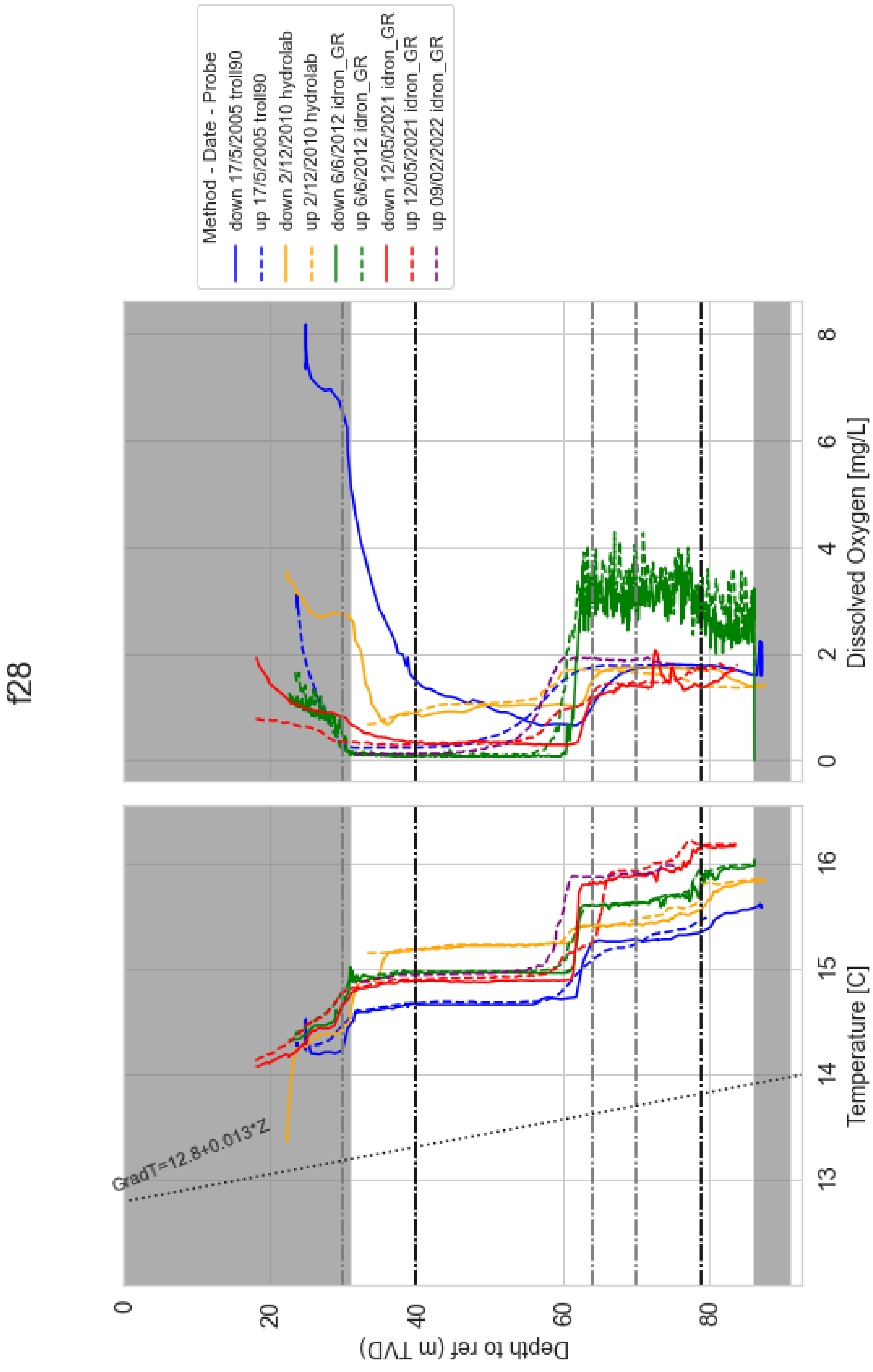
f28
Method - Date - Probe
down 17/5/2005 troll90
up 17/5/2005 troll90
down 2/12/2010 hydrolab
up 2/12/2010 hydrolab
down 6/6/2012 idron_GR
up 6/6/2012 idron_GR
down 12/05/2021 idron_GR
up 12/05/2021 idron_GR
up 09/02/2022 idron_GR
Depth to ref (m TVD)
0
20
40
60
80
Temperature [C]
13
14
15
16
GradT=12.8+0.013*Z
Dissolved Oxygen [mg/L]
0
2
4
6
8

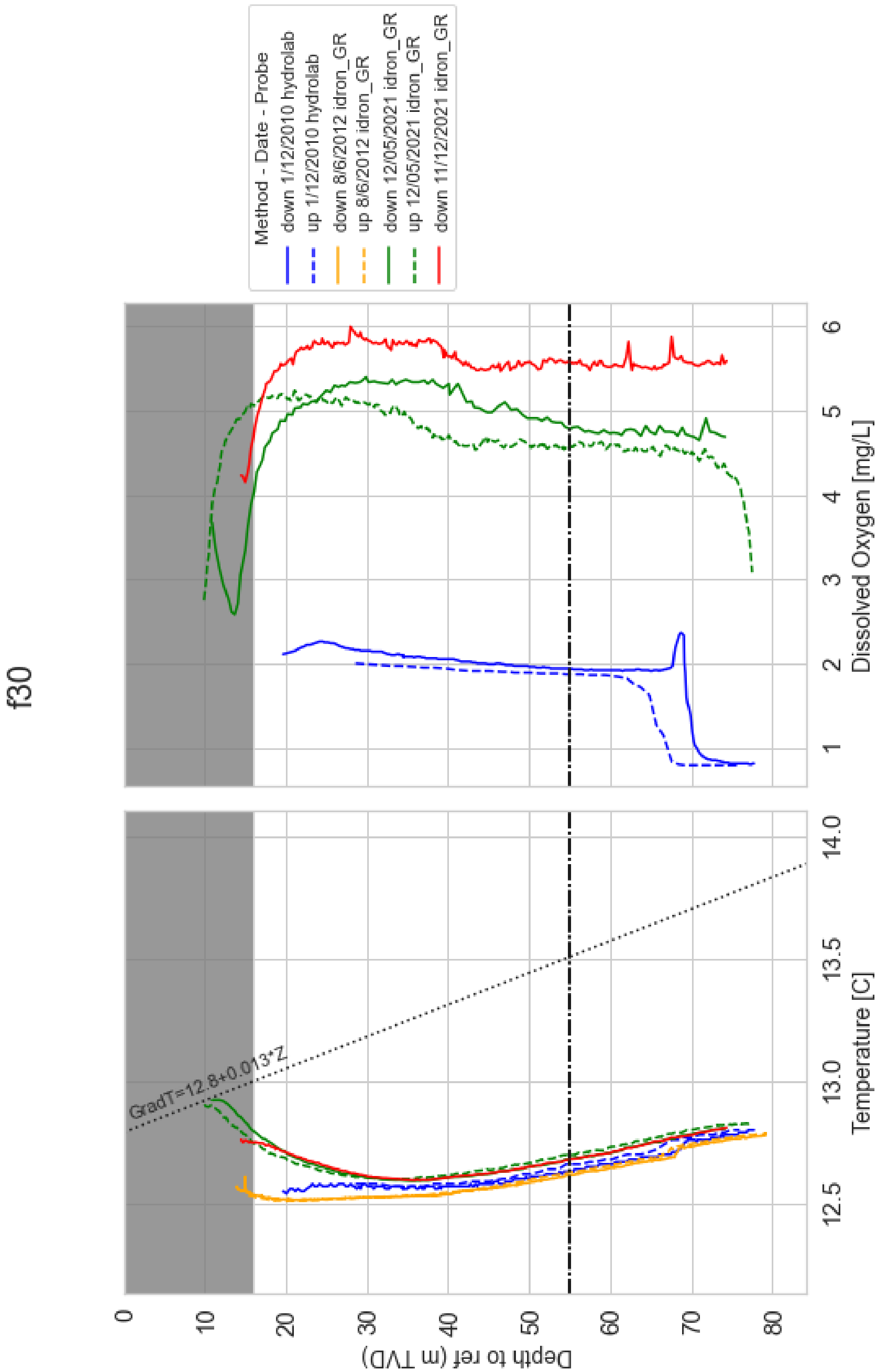
f30
Method - Date - Probe
down 1/12/2010 hydrolab
up 1/12/2010 hydrolab
down 8/6/2012 idron_GR
up 8/6/2012 idron_GR
down 12/05/2021 idron_GR
up 12/05/2021 idron_GR
down 11/12/2021 idron_GR
GradT=12.8+0.013*Z
Depth to ref (m TVD)
Temperature [C]
Dissolved Oxygen [mg/L]
0
10
20
30
40
50
60
70
80
12.5
13.0
13.5
14.0
1
2
3
4
5
6

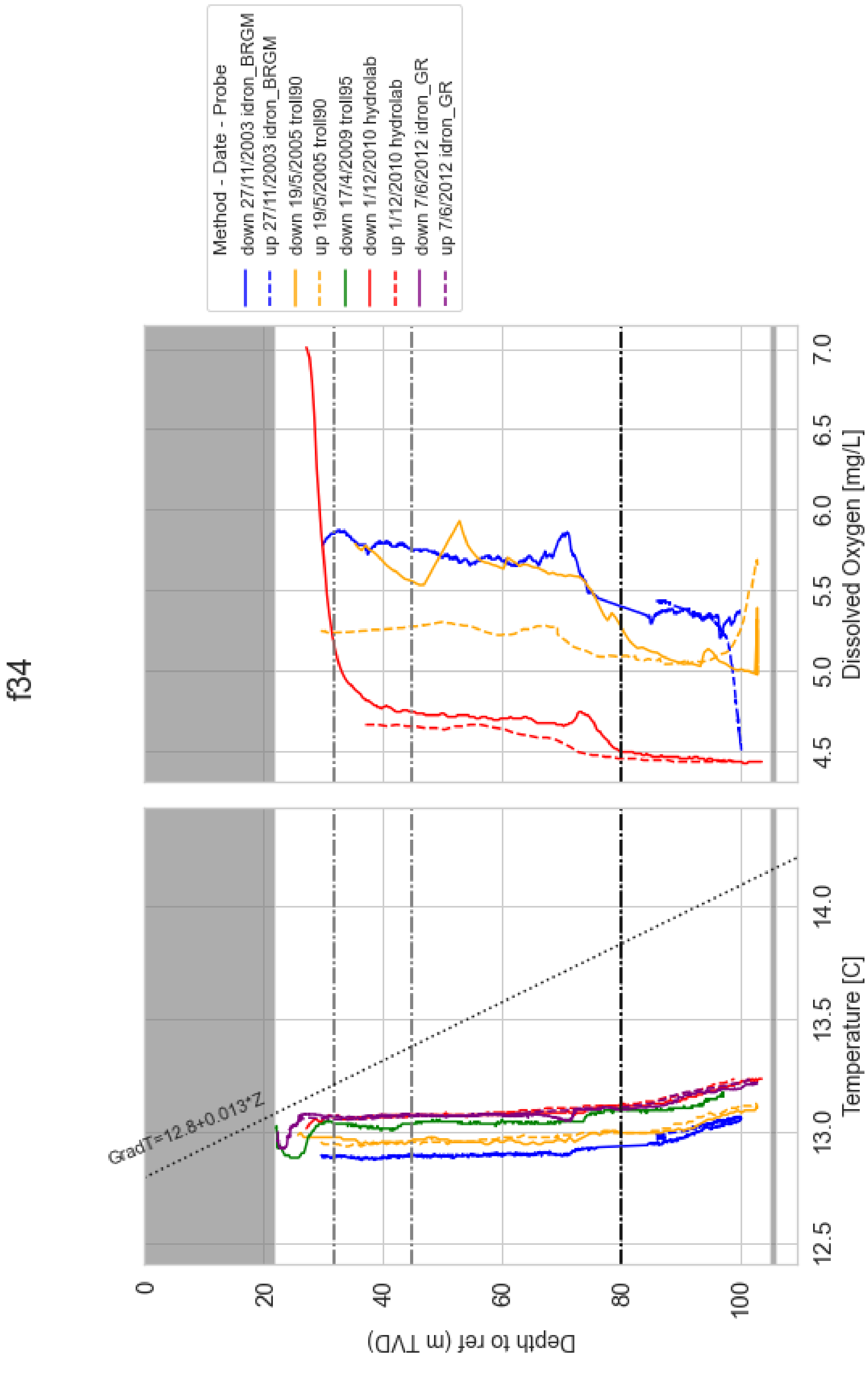
f34
Method - Date - Probe
down 27/11/2003 idron_BRGM
up 27/11/2003 idron_BRGM
down 19/5/2005 troll90
up 19/5/2005 troll90
down 17/4/2009 troll95
down 1/12/2010 hydrolab
up 1/12/2010 hydrolab
down 7/6/2012 idron_GR
up 7/6/2012 idron_GR
GradT=12.8+0.013*Z
Depth to ref (m TVD)
0
20
40
60
80
100
12.5
13.0
13.5
14.0
Temperature [C]
4.5
5.0
5.5
6.0
6.5
7.0
Dissolved Oxygen [mg/L]

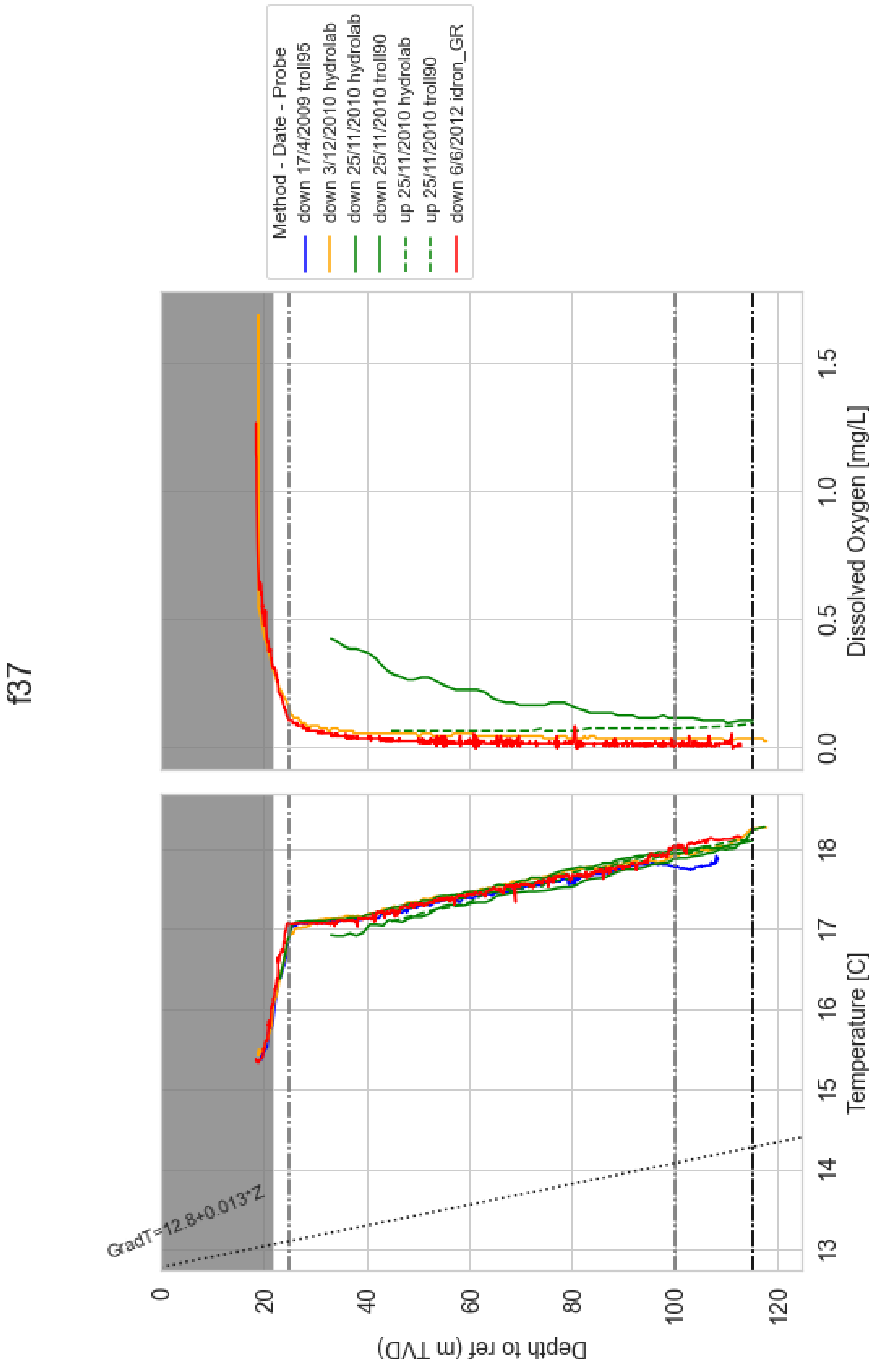
f37
GradT=12.8+0.013*Z
Depth to ref (m TVD)
0
20
40
60
80
100
120
13
14
15
16
17
18
Temperature [C]
0.0
0.5
1.0
1.5
Dissolved Oxygen [mg/L]
Method - Date - Probe
down 17/4/2009 troll95
down 3/12/2010 hydrolab
down 25/11/2010 hydrolab
down 25/11/2010 troll90
up 25/11/2010 hydrolab
up 25/11/2010 troll90
down 6/6/2012 idron_GR

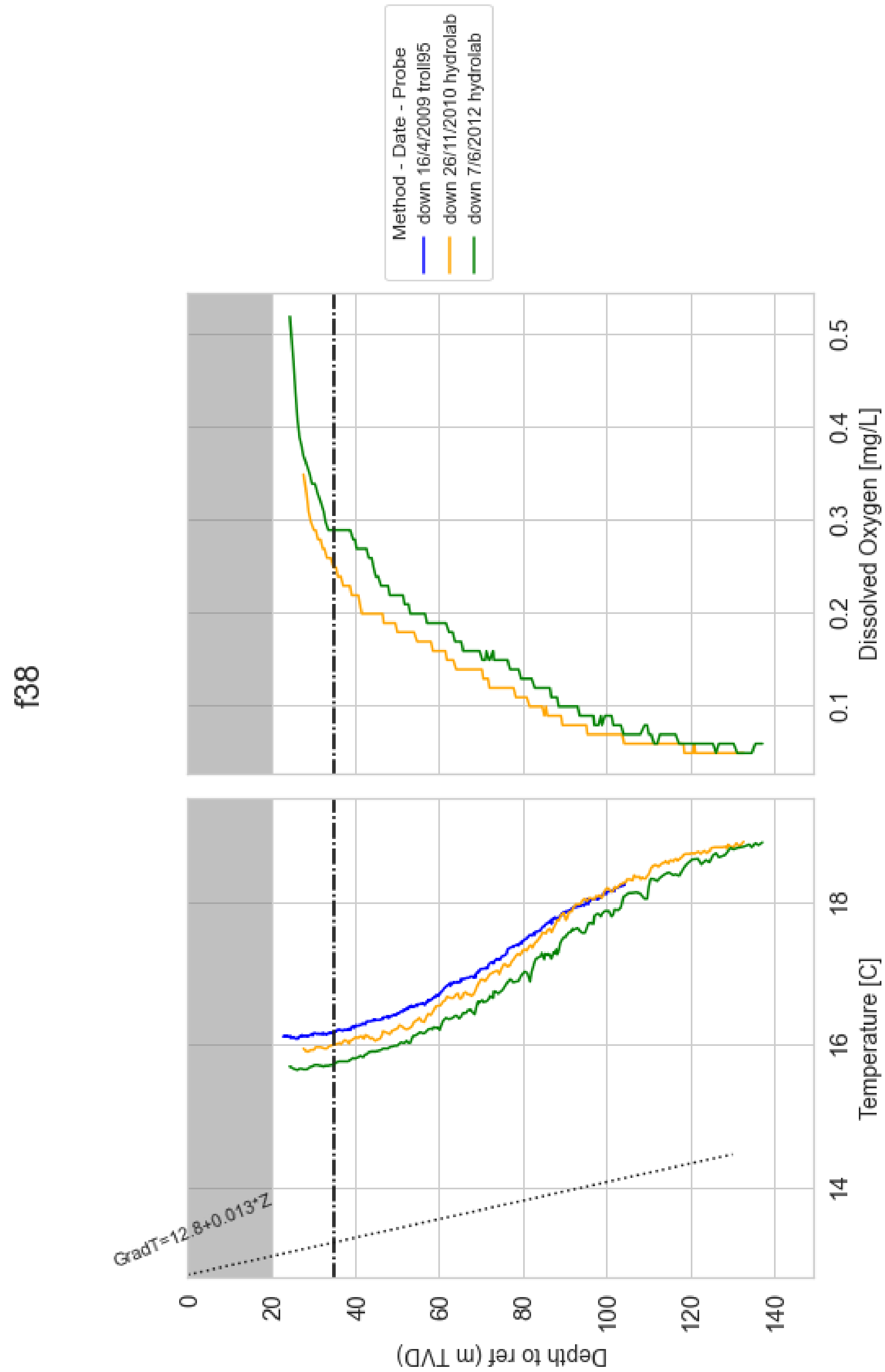
f38
Method - Date - Probe
down 16/4/2009 troll95
down 26/11/2010 hydrolab
down 7/6/2012 hydrolab
GradT=12.8+0.013*Z
Depth to ref (m TVD)
0
20
40
60
80
100
120
140
14
16
18
Temperature [C]
0.1
0.2
0.3
0.4
0.5
Dissolved Oxygen [mg/L]

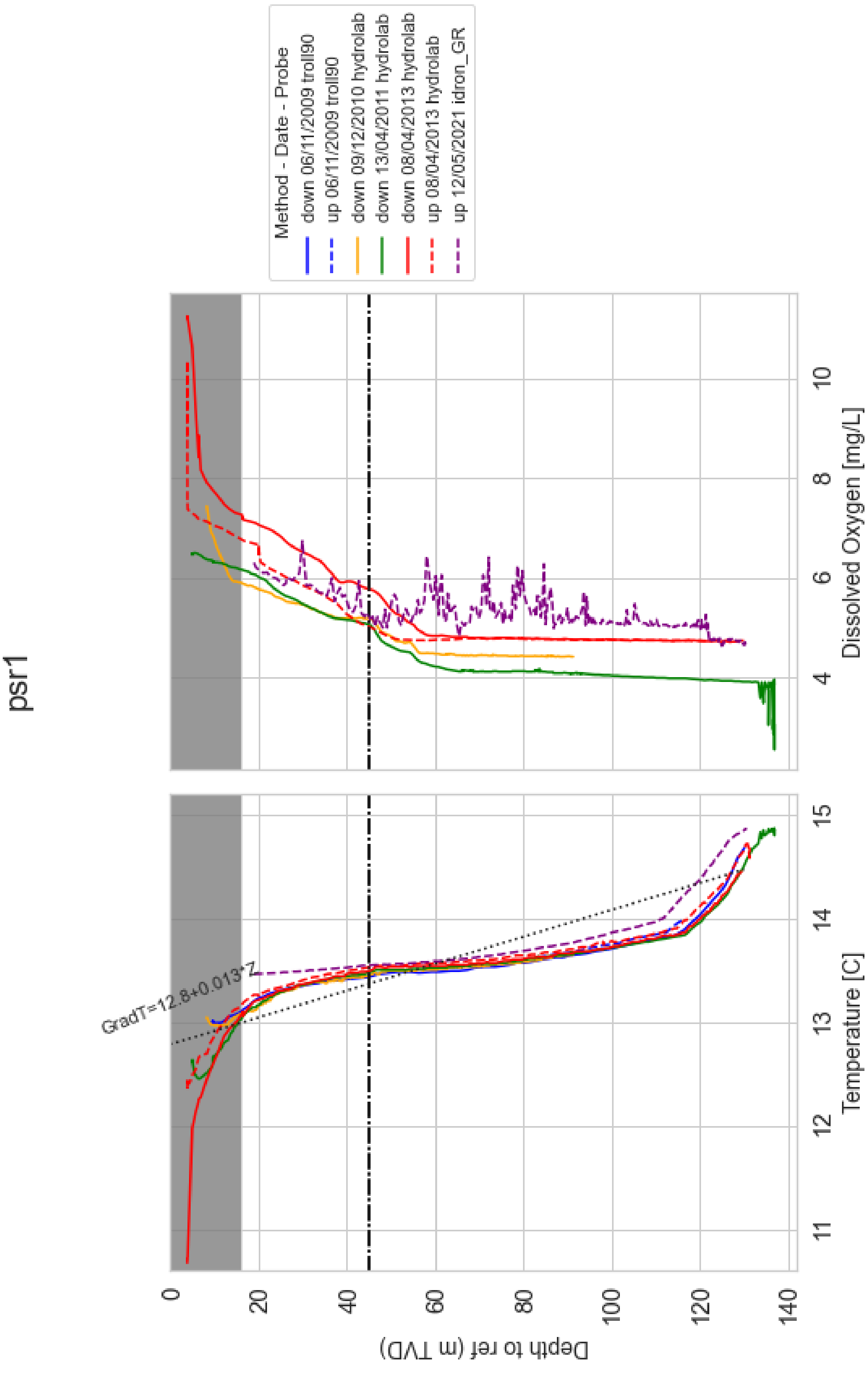
psr1
Method - Date - Probe
down 06/11/2009 troll90
up 06/11/2009 troll90
down 09/12/2010 hydrolab
down 13/04/2011 hydrolab
down 08/04/2013 hydrolab
up 08/04/2013 hydrolab
up 12/05/2021 idron_GR
GradT=12.8+0.013*Z
Depth to ref (m TVD)
Temperature [C]
Dissolved Oxygen [mg/L]

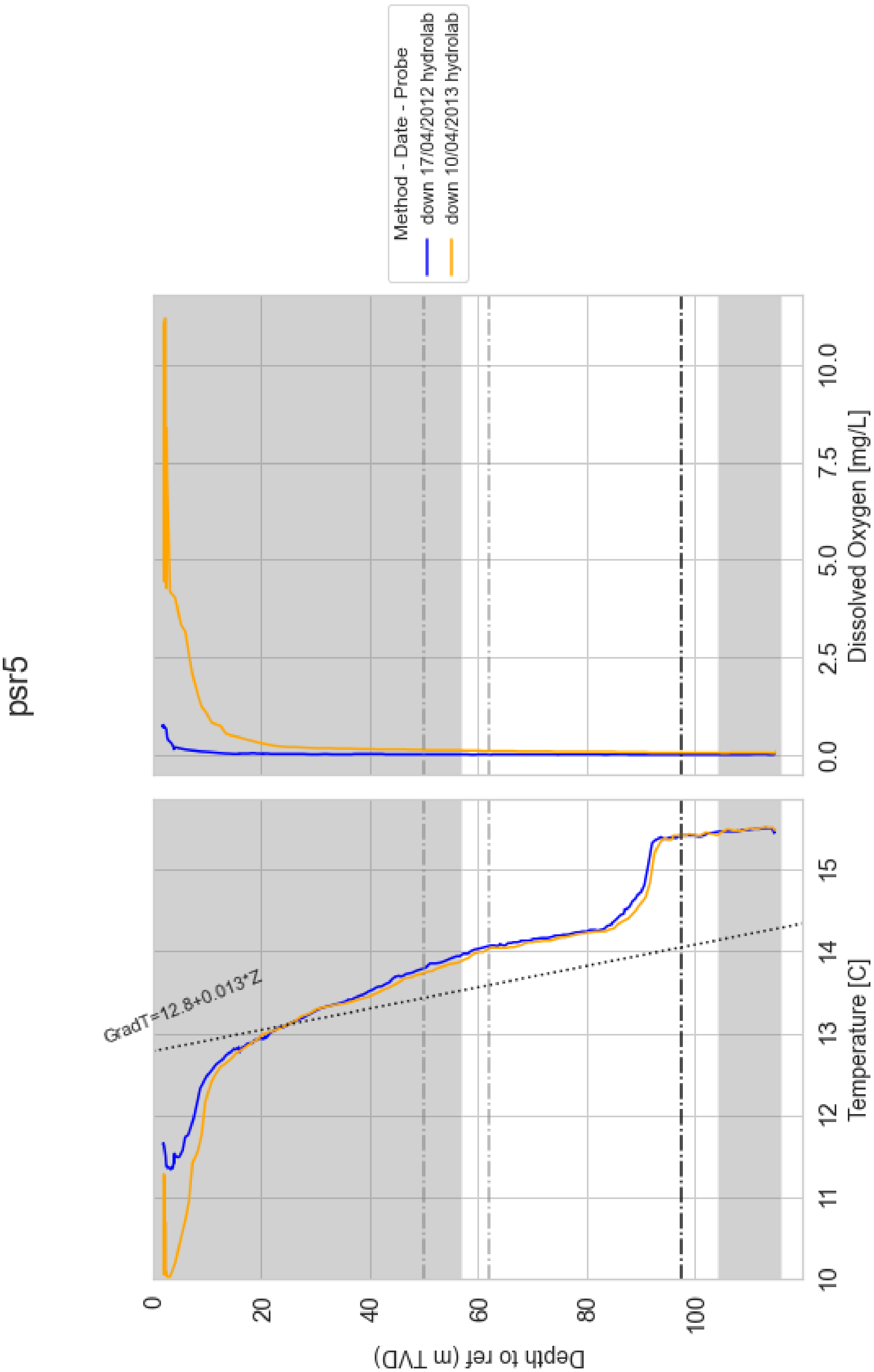
psr5
Method - Date - Probe
down 17/04/2012 hydrolab
down 10/04/2013 hydrolab
GradT=12.8+0.013*Z
Depth to ref (m TVD)
Temperature [C]
Dissolved Oxygen [mg/L]

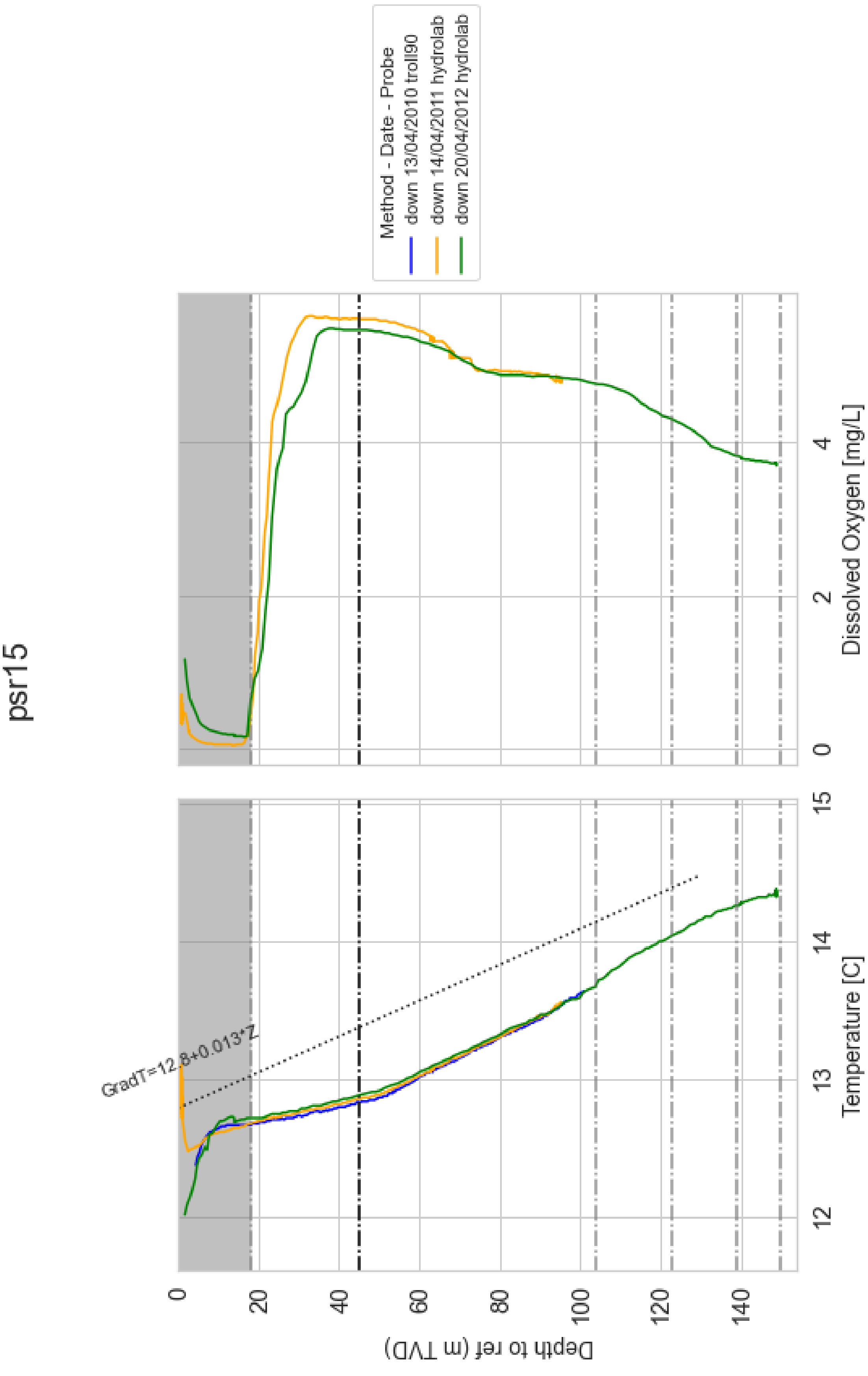
psr15
Method - Date - Probe
down 13/04/2010 troll90
down 14/04/2011 hydrolab
down 20/04/2012 hydrolab
GradT=12.8+0.013*Z
Depth to ref (m TVD)
Temperature [C]
Dissolved Oxygen [mg/L]
0
20
40
60
80
100
120
140
12
13
14
15
0
2
4

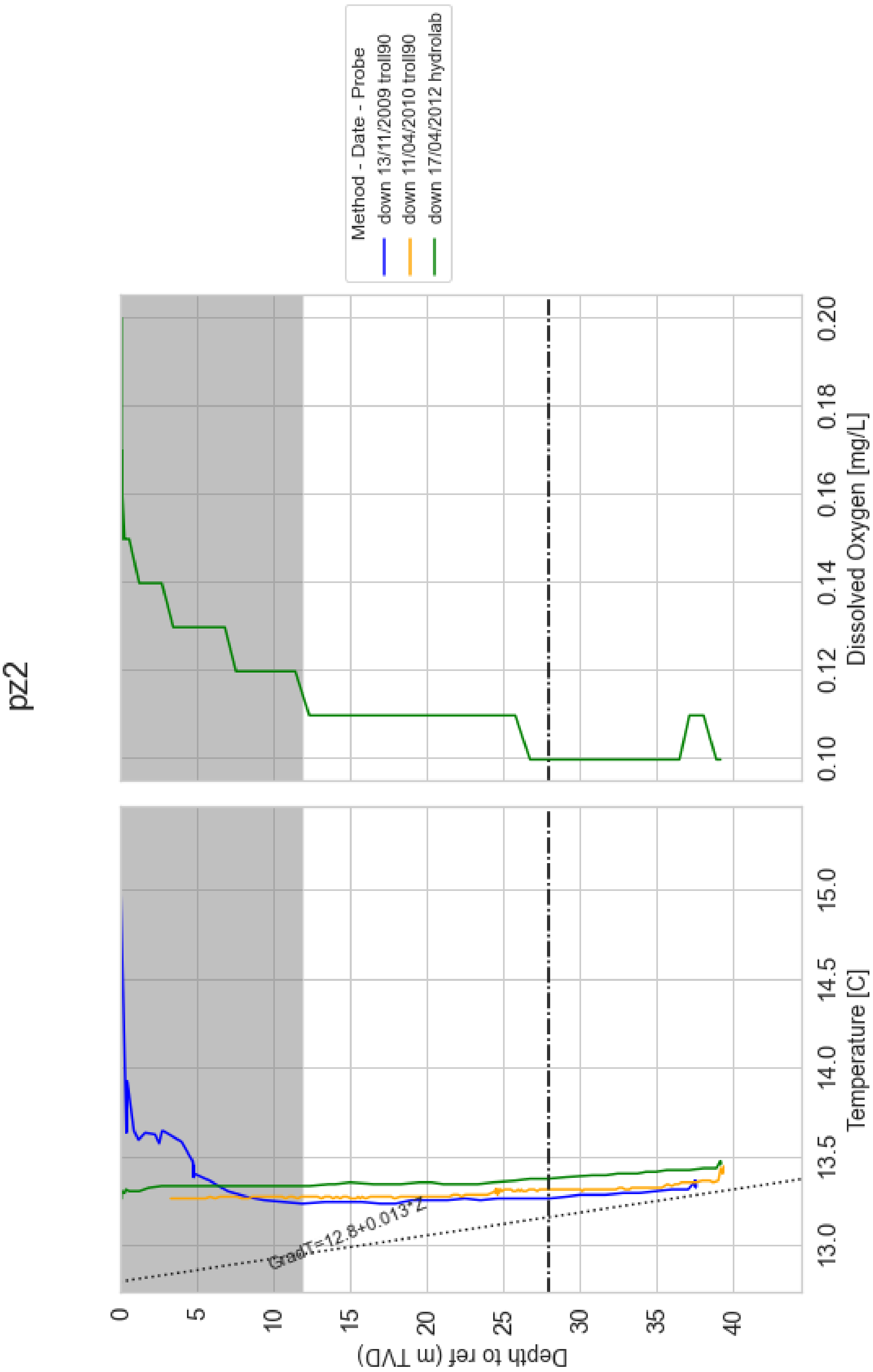
pz2
Method - Date - Probe
down 13/11/2009 troll90
down 11/04/2010 troll90
down 17/04/2012 hydrolab
GradT=12.8+0.013*Z
Temperature [C]
Dissolved Oxygen [mg/L]
Depth to ref (m TVD)
0
5
10
15
20
25
30
35
40
13.0
13.5
14.0
14.5
15.0
0.10
0.12
0.14
0.16
0.18
0.20

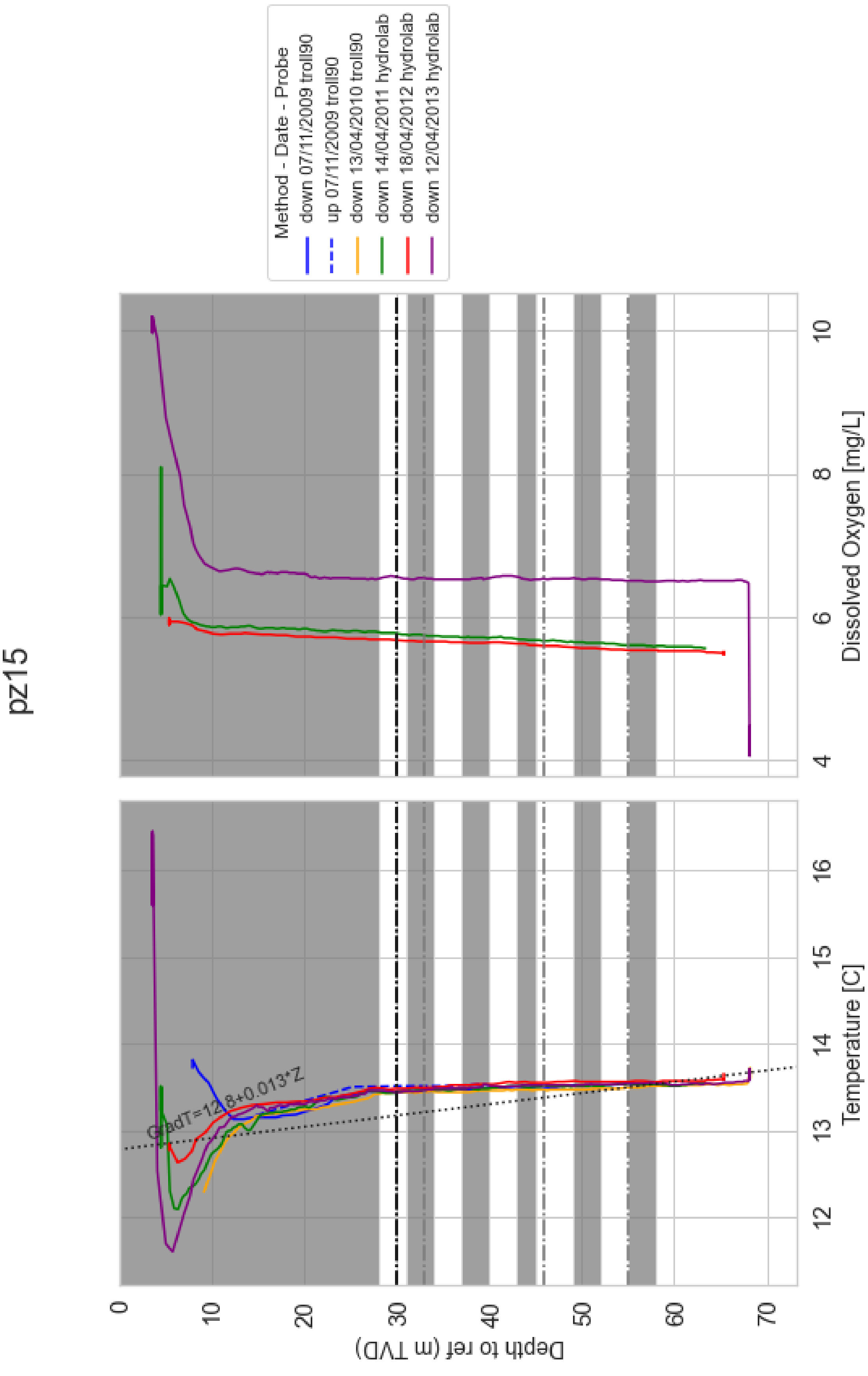
pz15
Method - Date - Probe
down 07/11/2009 troll90
up 07/11/2009 troll90
down 13/04/2010 troll90
down 14/04/2011 hydrolab
down 18/04/2012 hydrolab
down 12/04/2013 hydrolab
GradT=12.8+0.013*Z
Depth to ref (m TVD)
0
10
20
30
40
50
60
70
Temperature [C]
12
13
14
15
16
Dissolved Oxygen [mg/L]
4
6
8
10

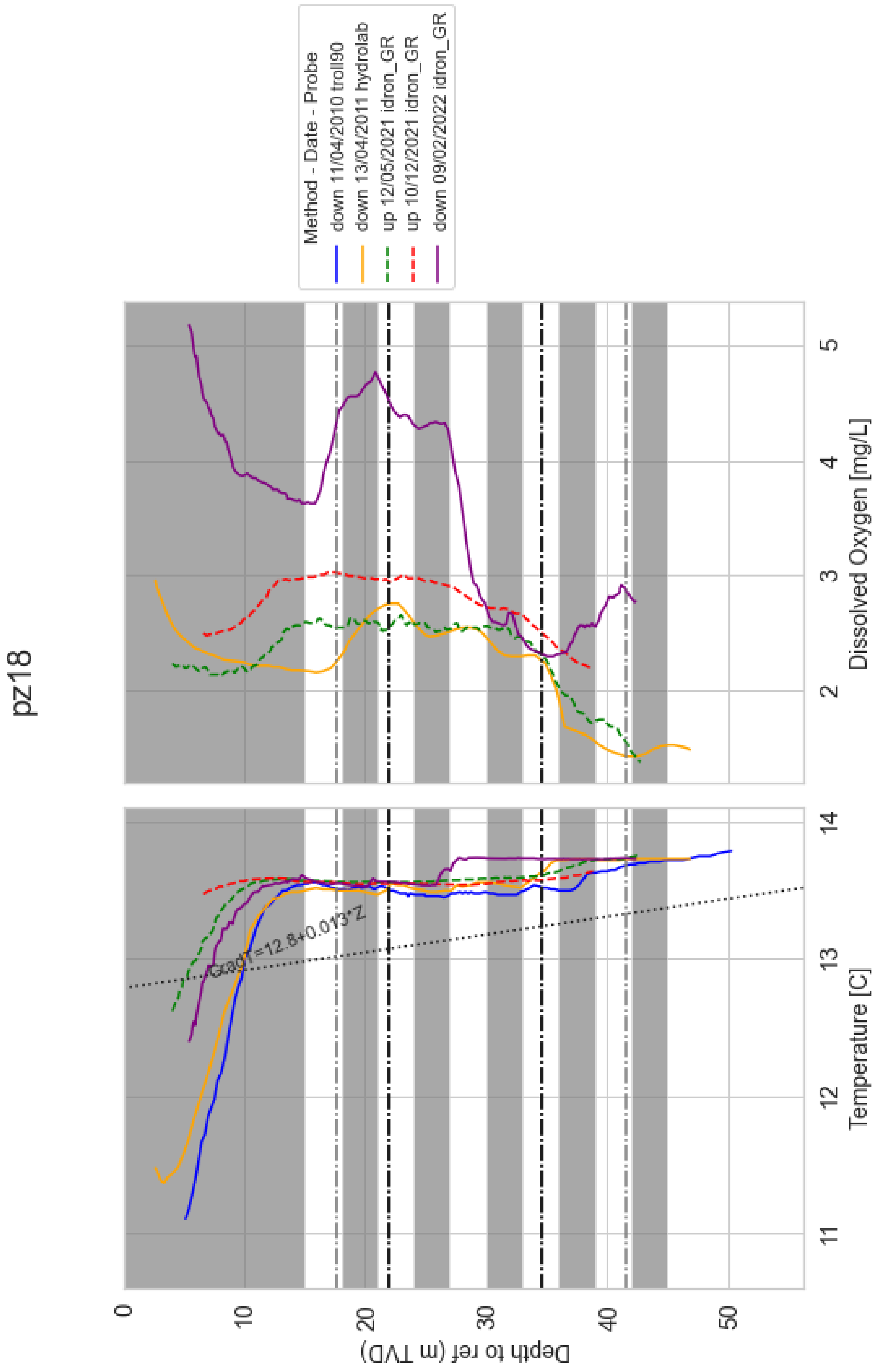
pz18
Method - Date - Probe
down 11/04/2010 troll90
down 13/04/2011 hydrolab
up 12/05/2021 idron_GR
up 10/12/2021 idron_GR
down 09/02/2022 idron_GR
Grad1=12.8+0.013*Z
Depth to ref (m TVD)
0
10
20
30
40
50
Temperature [C]
11
12
13
14
Dissolved Oxygen [mg/L]
2
3
4
5

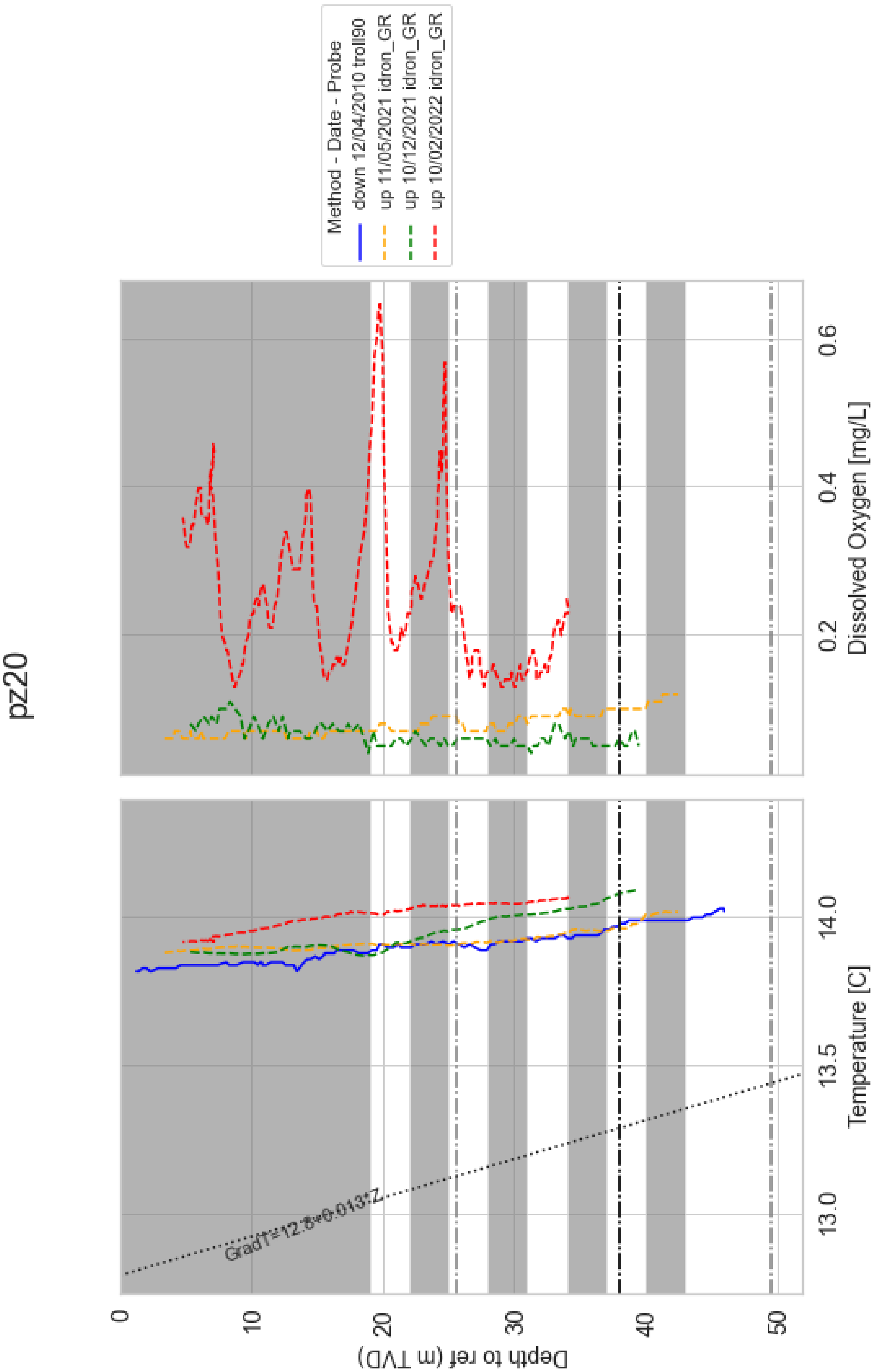
pz20
Method - Date - Probe
down 12/04/2010 troll90
up 11/05/2021 idron_GR
up 10/12/2021 idron_GR
up 10/02/2022 idron_GR
Dissolved Oxygen [mg/L]
Temperature [C]
Depth to ref (m TVD)
GradT=12.8+0.013*Z

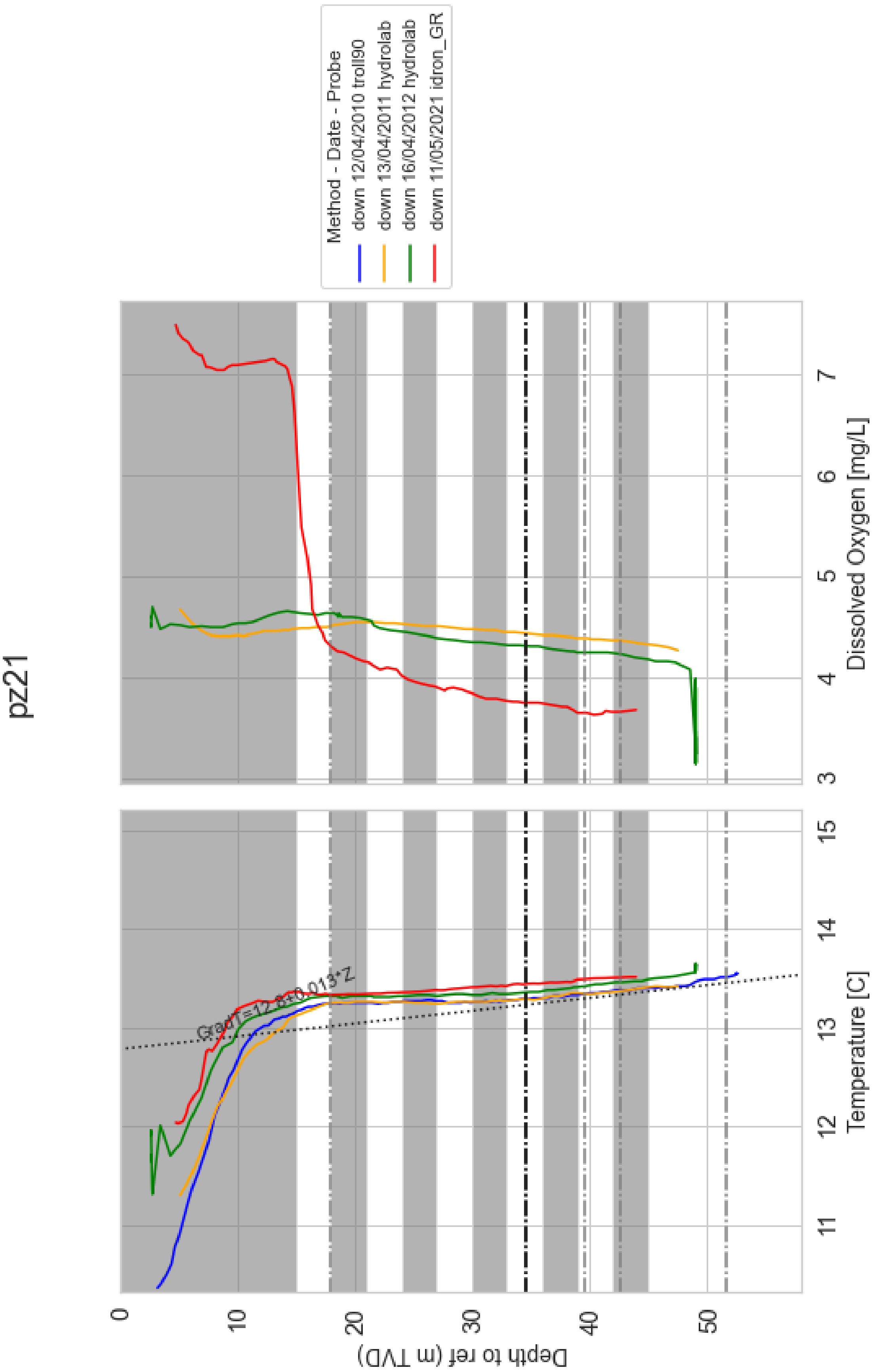
pz21
Method - Date - Probe
down 12/04/2010 troll90
down 13/04/2011 hydrolab
down 16/04/2012 hydrolab
down 11/05/2021 idron_GR
GradT=12.8+0.013*Z
Temperature [C]
Dissolved Oxygen [mg/L]
Depth to ref (m TVD)

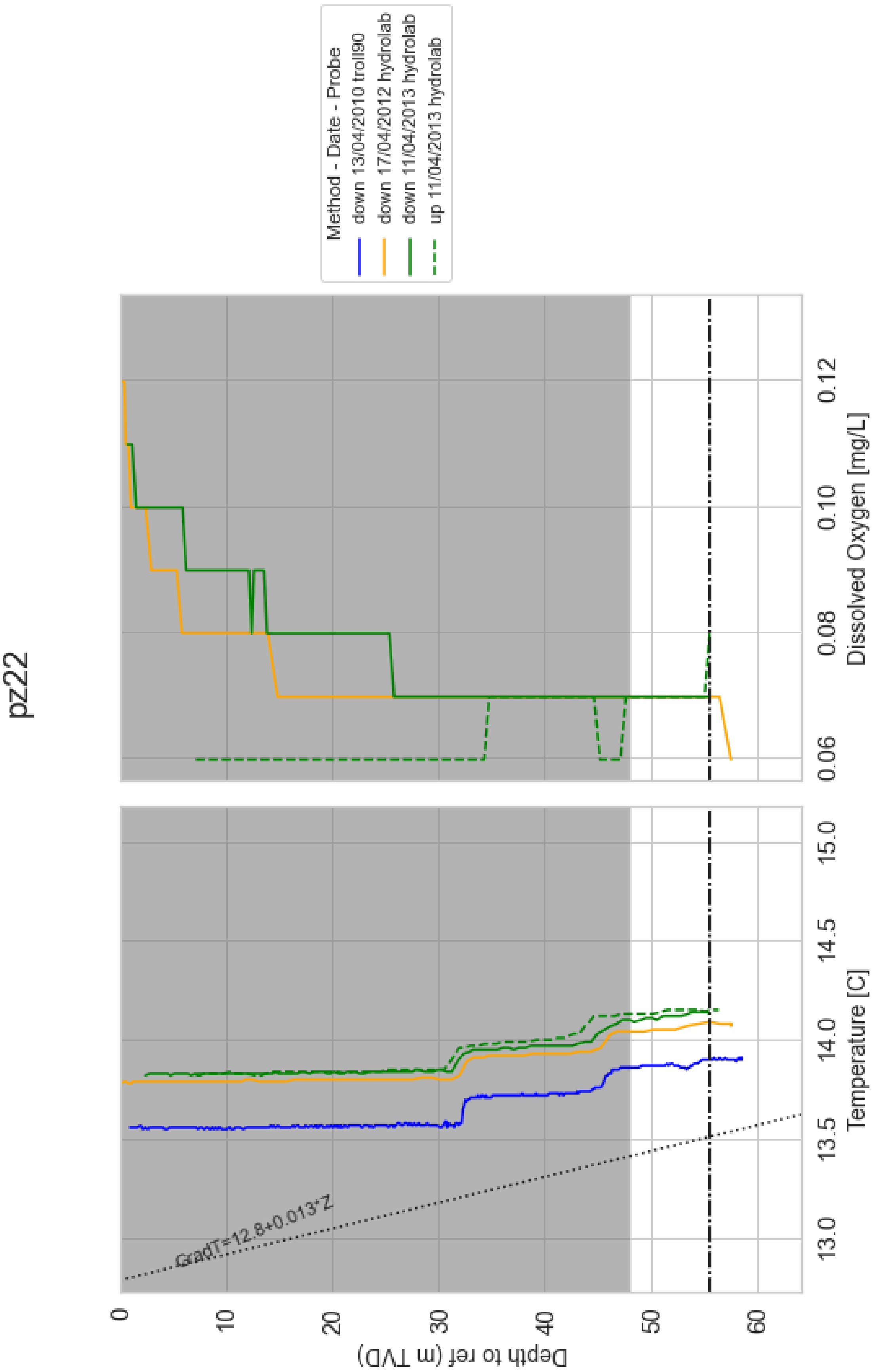
pz22
Method - Date - Probe
down 13/04/2010 troll90
down 17/04/2012 hydrolab
down 11/04/2013 hydrolab
up 11/04/2013 hydrolab
Dissolved Oxygen [mg/L]
0.06
0.08
0.10
0.12
Temperature [C]
13.0
13.5
14.0
14.5
15.0
GradT=12.8+0.013*Z
Depth to ref (m TVD)
0
10
20
30
40
50
60

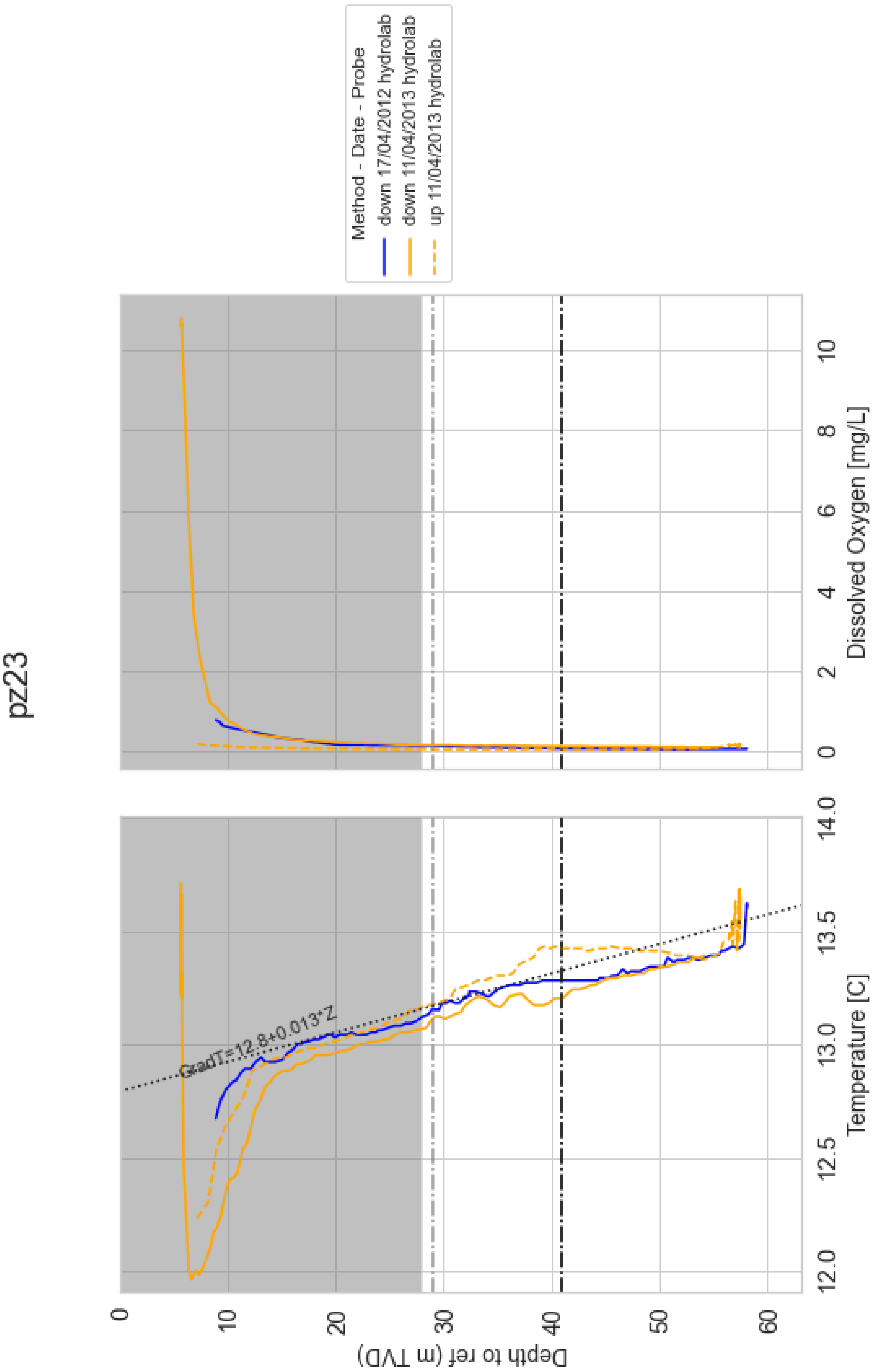
pz23
Method - Date - Probe
down 17/04/2012 hydrolab
down 11/04/2013 hydrolab
up 11/04/2013 hydrolab
GradT=12.8+0.013*Z
Depth to ref (m TVD)
Temperature [C]
Dissolved Oxygen [mg/L]
0
10
20
30
40
50
60
12.0
12.5
13.0
13.5
14.0
0
2
4
6
8
10

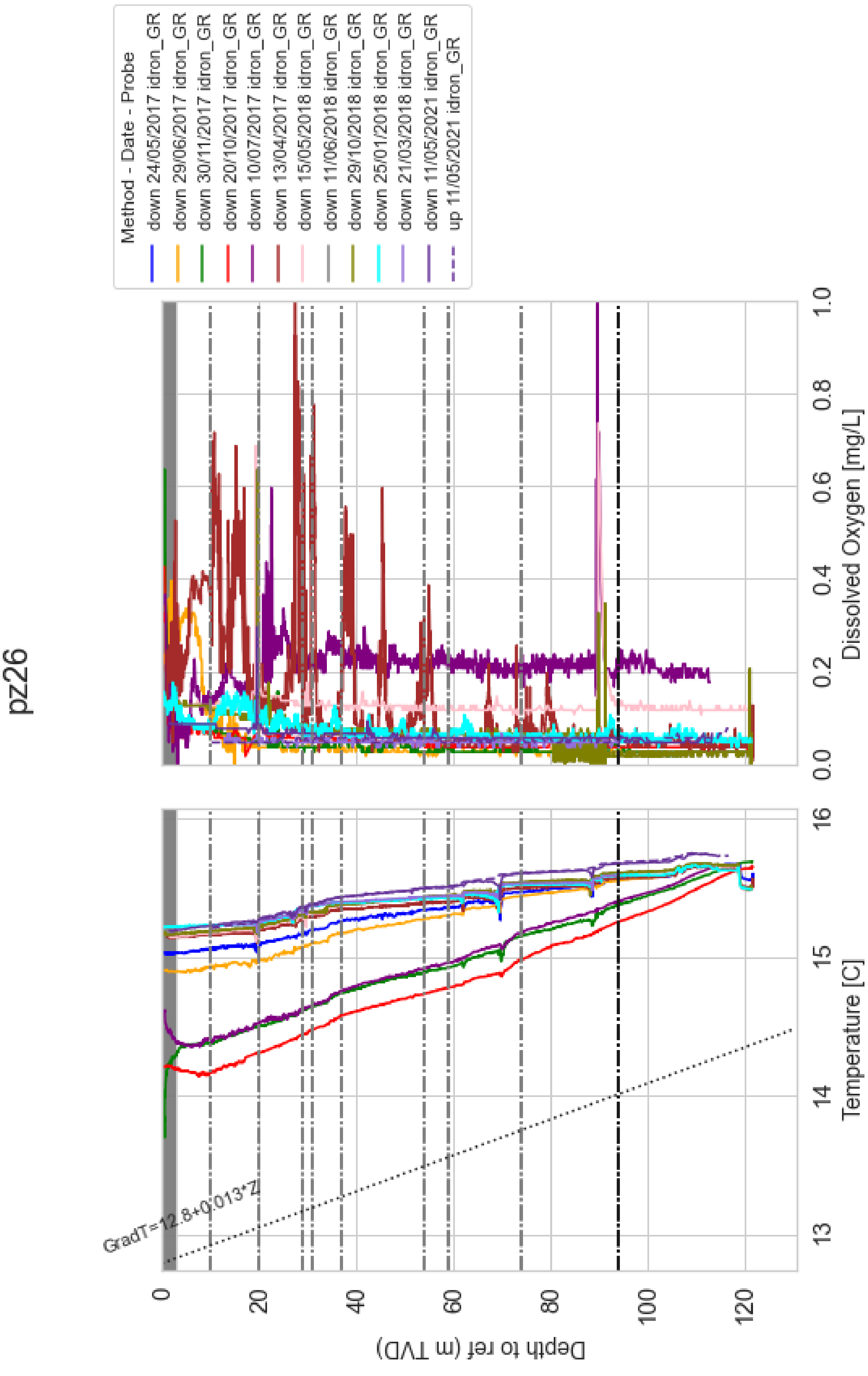

pz26
Method - Date - Probe
down 24/05/2017 idron_GR
down 29/06/2017 idron_GR
down 30/11/2017 idron_GR
down 20/10/2017 idron_GR
down 10/07/2017 idron_GR
down 13/04/2017 idron_GR
down 15/05/2018 idron_GR
down 11/06/2018 idron_GR
down 29/10/2018 idron_GR
down 25/01/2018 idron_GR
down 21/03/2018 idron_GR
down 11/05/2021 idron_GR
up 11/05/2021 idron_GR
Dissolved Oxygen [mg/L]
0.0
0.2
0.4
0.6
0.8
1.0
Temperature [C]
13
14
15
16
GradT=12.8+0.013*Z
Depth to ref (m TVD)
0
20
40
60
80
100
120

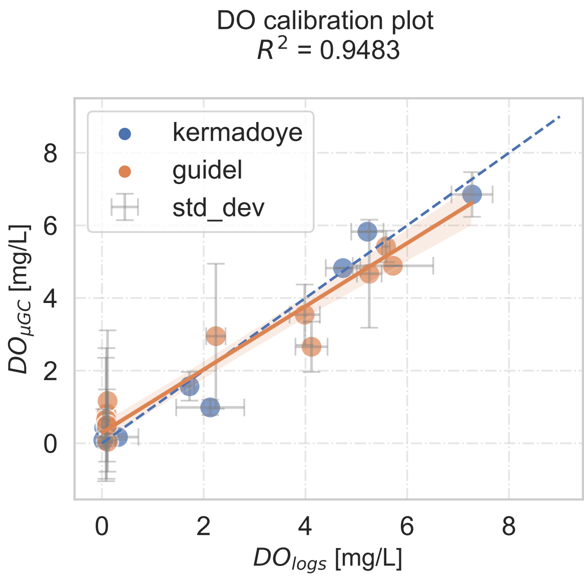

Figure 3. Calibration plot for DO measurements with the multiparameter probe (logs) vs gas chromatography (μGC) analysis made on the same samples.

References

Blanc, P., Lassin, A., Piantone, P., Azaroual, M., Jacquemet, N., Fabbri, A., & Gaucher, E. C. (2012). Thermoddem: A geochemical database focused on low temperature water/rock interactions and waste materials. *Applied Geochemistry*, *27*(10), 2107–2116. Retrieved from `http://dx.doi.org/10.1016/j.apgeochem.2012.06.002` doi: 10.1016/j.apgeochem.2012.06.002

Bochet, O., Bethencourt, L., Dufresne, A., Farasin, J., Pédrot, M., Labasque, T., . . . Le Borgne, T. (2020, feb). Iron-oxidizer hotspots formed by intermittent oxic–anoxic fluid mixing in fractured rocks. *Nature Geoscience*, *13*(2), 149–155. doi: 10.1038/s41561-019-0509-1

Klepikova, M. V., Le Borgne, T., Bour, O., & Davy, P. (2011). A methodology for using borehole temperature-depth profiles under ambient, single and cross-borehole pumping conditions to estimate fracture hydraulic properties. *Journal of Hydrology*, *407*(1-4), 145–152. Retrieved from `http://dx.doi.org/10.1016/j.jhydrol.2011.07.018` doi: 10.1016/j.jhydrol.2011.07.018

Le Borgne, T., Paillet, F., Bour, O., & Caudal, J. P. (2006). Cross-borehole flowmeter tests for transient heads in heterogeneous aquifers. *Ground Water*, *44*(3), 444–452. doi: 10.1111/j.1745-6584.2005.00150.x

Palandri, J., & Kharaka, Y. (2004). *A Compilation of Rate Parameters of Water-Mineral Interaction Kinetics* (Vol. REPORT 200; Tech. Rep.).

Pouladi, B., Bour, O., Longuevergne, L., de La Bernardie, J., & Simon, N. (2021). Modelling borehole flows from Distributed Temperature Sensing data to monitor groundwater dynamics in fractured media. *Journal of Hydrology*, *598*(November 2020). doi: 10.1016/j.jhydrol.2021.126450

Ruelleu, S., Moreau, F., Bour, O., Gapais, D., & Martelet, G. (2010). Impact of gently dipping discontinuities on basement aquifer recharge: An example from Ploemeur (Brittany, France). *Journal of Applied Geophysics*, *70*(2), 161–168. Retrieved from `http://dx.doi.org/10.1016/j.jappgeo.2009.12.007` doi:

10.1016/j.jappgeo.2009.12.007